Enhanced Light–Matter Interaction and Polariton Relaxation by the Control of Molecular Orientation

Tomohiro Ishii, Fatima Bencheikh, Sébastien Forget, Sébastien Chénais, Benoît Heinrich, David Kreher, Lydia Sosa Vargas, Kiyoshi Miyata, Ken Onda, Takashi Fujihara, et al.

To cite this version:

Tomohiro Ishii, Fatima Bencheikh, Sébastien Forget, Sébastien Chénais, Benoît Heinrich, et al.. Enhanced Light–Matter Interaction and Polariton Relaxation by the Control of Molecular Orientation. Advanced Optical Materials, 2021, 9 (22), pp.2101048. ⟨10.1002/adom.202101048⟩. ⟨hal-03966978⟩

HAL Id: hal-03966978

https://hal.science/hal-03966978v1

Submitted on 1 Feb 2023

Enhanced light-matter interaction and polariton relaxation by the control of molecular orientation

Tomohiro Ishii[1], *Fatima Bencheikh*[1], *Sébastien Forget*[2], *Sébastien Chénais*[2], *Benoit Heinrich*[3], *David Kreher*[4,5], *Lydia Sosa Vargas*[4], *Kiyoshi Miyata*[6], *Ken Onda*[6], *Takashi Fujihara*[1], *Stéphane Kéna-Cohen*[7], *Fabrice Mathevet*[1,4*], *and Chihaya. Adachi*[1,8*]

Mr. Tomohiro Ishii, Dr. Fatima Bencheikh, Dr. Takashi Fujihara

1. Center for Organic Photonics and Electronics Research (OPERA) and Department of Applied Chemistry, Kyushu University, 744 Motooka, Nishi, Fukuoka 819-0395, Japan.

Prof. Sébastien Forget, Prof. Sébastien Chénais

2. Laboratoire de Physique des Lasers (LPL), Université Sorbonne Paris Nord, CNRS, UMR 7538, F-93430 Villetaneuse, France.

Prof. Benoit Heinrich

3. Institut de Physique et Chimie des Matériaux de Strasbourg (IPCMS), UMR 7504, CNRS-Université de Strasbourg, 23 Rue du Loess, 67034 Strasbourg Cedex 2, France.

Prof. David Kreher,

4. Sorbonne Université, Faculté des Sciences, CNRS, Institut Parisien de Chimie Moléculaire (IPCM), UMR 8232, 4 Place Jussieu, 75005 Paris, France.
5. Institut Lavoisier de Versailles (ILV), UMR-CNRS 8180, Université de Versailles-Saint-Quentin-en-Yvelines, 45 avenue des Etats-Unis, 78035 Versailles cedex, France.

Dr. Lydia Sosa Vargas

4. Sorbonne Université, Faculté des Sciences, CNRS, Institut Parisien de Chimie Moléculaire (IPCM), UMR 8232, 4 Place Jussieu, 75005 Paris, France.

Prof. Kiyoshi Miyata and Prof. Ken Onda

6. Department of Chemistry, Kyushu University, 744 Motooka, Nishi, Fukuoka 819-0395, Japan.

Prof. Stéphane Kéna-Cohen

7. Department of Engineering Physics, École Polytechnique de Montréal, Montréal H3C 3A7, QC, Canada.

Dr. Fabrice Mathevet (E-mail: fabrice.mathevet@sorbonne-universite.fr)

1. Center for Organic Photonics and Electronics Research (OPERA) and Department of Applied Chemistry, Kyushu University, 744 Motooka, Nishi, Fukuoka 819-0395, Japan.
4. Sorbonne Université, Faculté des Sciences, CNRS, Institut Parisien de Chimie Moléculaire (IPCM), UMR 8232, 4 Place Jussieu, 75005 Paris, France.

Prof. Chihaya Adachi (E-mail: adachi@cstf.kyushu-u.ac.jp)

1. Center for Organic Photonics and Electronics Research (OPERA) and Department of Applied Chemistry, Kyushu University, 744 Motooka, Nishi, Fukuoka 819-0395, Japan.

8. International Institute for Carbon Neutral Energy Research (WPI-I2CNER), Kyushu University, 744 Motooka, Nishi, Fukuoka 819-0395, Japan.

Keywords: (exciton-polariton; microcavities; liquid crystal; molecular orientation; polariton relaxation)

Abstract:

Exciton-polaritons, in which the electronic state of an excited organic molecule and a photonic state are strongly coupled, can form a Bose-Einstein condensate (BEC) at room temperature. However, so far, the reported thresholds of organic polariton BECs under optical excitation are as high as $P_{\mathrm{th}} \sim 11$ - 500 μJ cm^{-2}. One route towards lowering the condensation threshold is to increase the Rabi energy by aligning the molecular transition dipole moments. In this report, we demonstrate that control of the orientation of a perylene-based discotic dye, which is able to self-organize in mesogenic columnar structures, can significantly enhance exciton-photon interaction and polariton relaxation rate in optical cavities. These results show the importance of the molecular orientation for strong light–matter interactions and provide a promising strategy toward the realization of an organic low threshold polariton laser system and electrically driven organic polariton BEC. [143 words]

MAIN TEXT:

1. Introduction

Exciton-polaritons are the bosonic quasiparticles resulting from the light-matter strong coupling between the exciton and photons confined in microcavities. In this strong coupling regime, the interaction between the exciton and a resonant electromagnetic mode gives rise to hybrid excited states which are characterized by an energy level splitting. These states form the upper polariton (UP) and the lower polariton (LP) branches, with a minimum splitting called the Rabi splitting.[1-2] For Wannier-Mott excitons in group III-V semiconductors, the Rabi splitting is typically in the 5-10 meV range.[3-7] On the other hand, for Frenkel excitons in organic microcavities, the Rabi splitting can be 10-100 times larger than the splitting in the inorganic microcavities due to their large binding energy.[8-11] The large Rabi splitting achievable in organic microcavities allows for strong coupling and polariton BEC to be realized at room temperature.[12-16] Very recently, important advances such as the development of strongly coupled light-emitting field-effect transistors based on electrical pumping of exciton-polaritons at room temperature have been demonstrated, providing a route toward quantum optoelectronic applications.[17] However, so far, the reported thresholds of organic polariton BECs under optical excitation are as high as $P_{th} \sim 11$ - 500 μJ cm^{-2}.[12-16, 51-52] As a result, electrically driven organic polariton BEC, which paves ways for many practical applications, has not been achieved yet.

The efficiency of polariton relaxation is a critical issue for further reducing the BEC threshold.[18] After excitation, relaxation from the exciton reservoir to the lower polariton branch can occur through different scattering processes. In the case of organic molecules, this relaxation is thought to be dominated by luminescence and vibrationally-assisted relaxation.[18-21]

The properties of exciton-polaritons depend on the intrinsic properties of the organic molecules, such as their photoluminescence quantum yield (PLQY), vibrational modes and oscillator strength. The Rabi splitting, which is a measure of the light-matter interaction strength, depends on the number of molecules within the cavity, the optical mode volume on resonance and the projection of the transition dipole moment along mode's electric field orientation.[22] Non-equilibrium models for condensation have shown that the threshold is reduced for increasing values of the Rabi splitting.[23] Aligning molecules along the electric field orientation can thus be used as a strategy to reduce condensation thresholds. To date, most of strongly coupled light–matter systems have been based on amorphous materials [8, 9, 11, 14-16, 52] and only few works are based on anisotropic systems such as organic single crystals[10,12,24,25, 51] or aligned nanotubes[26] and π-conjugated polymers[27,28].

As archetypical anisotropic systems, liquid crystalline semiconductors have been attracting a strong interest for organic electronic and photonic devices. [29-30,32-36,46-48] These materials offer the advantage of controlling the order in bulk and at interfaces at all length scales from molecular to macroscopic distances. Among the various liquid crystalline materials, discotic liquid crystal (DLC) received a particular attention for optoelectronic applications. Consisting of π-conjugated disk-shaped central cores substituted with peripheral flexible aliphatic chains, these materials self-organize into columnar structures, which can be easily oriented with the column direction parallel or perpendicular to the substrate via specific surface alignment layers.[37,49-50] In this context, a microcavity with perfectly oriented DLC semiconductors is an ideal system for studying the relationship between the transition dipole moment orientation and polariton formation dynamics.

In this work, we demonstrate that the control of the orientation of a liquid crystalline perylene bisimide semiconductor can significantly enhance the light-matter interaction strength and the polariton relaxation efficiency in optical cavities. Exciton-polaritons are observed by angle-resolved reflectance and angle-resolved photoluminescence (PL), and these measurements show the anisotropy of the Rabi splitting due to the large polarization anisotropy of the liquid crystal semiconductor. We also investigate polariton relaxation through transient PL, and demonstrate that polariton relaxation rate is doubled in the microcavity filled with in-plane orientation of perylene molecules in comparison with their edge-on orientation. These results evidence the importance of the molecular orientation for strong light–matter interactions, providing a route toward realization of low threshold polariton lasing in 1D photonic crystals.

2. Result & Discussion

The structure of the liquid crystalline perylene bisimide emitter (PBLC) is given in **Fig**. 1a. It consists of a 1,6,7,12-tetra-4-nonylphenoxy perylene bisimide (PBI) with two dodecyl chains at the imide positions. This discotic emitter was specifically designed to possess a high PLQY and a columnar organization in the solid state maintained at room temperature. To this end, 4-nonylphenoxy groups grafted in the bay position of the PBI core were chosen as a mixture of branched isomers to increase the alkyl chain entropy and prevent the crystallization of the compound at room temperature. [38,39] The synthesis of PBLC is described in Supporting Information. The direction of the transition dipole moment of the PBLC is in the plane of the molecule, along the long molecular axis, owing to the molecular orbitals of perylene bisimides. [40,41]

The thermal behavior of PBLC was investigated by differential scanning calorimetry (DSC), polarizing optical microscopy (POM), and X-ray Scattering (SWAXS). The DSC traces recorded on heating from -20°C to 200°C at 10 °C/min show only one phase transition at 156 °C with an associated transition enthalpy about 6.8 J/g, suggesting a transition from a liquid crystal phase to the isotropic liquid phase (Fig. 1b). On cooling, the reversible transition was observed at 156 °C (ΔH = 6.8 J/g) and no additional thermal event was detected until -20 °C. Observed by POM, on the heating process, PBLC showed the highly birefringent optical texture characteristic of a mesophase until the transition to the isotropic phase, above 156 °C. On cooling from Iso, the compound gives well-developed pseudo focal-conic textures at 150 °C, which is a typical behavior of columnar mesophases (Fig. S2a). As shown in Fig. S2b, these textures are maintained at room temperature. These POM observations are consistent with the DSC measurements, confirming the absence of crystallization on cooling caused by the branched alkyl chains surrounding the PBI cores. Temperature-dependent X-ray scattering experiments confirmed the presence of the columnar mesophase between room temperature and 155°C. The small- and wide-angle scattering (SWAXS) pattern of PBLC contained the characteristic signals of a columnar structure such as the broad scattering from molten chain h_{ch}, the broadened peak from π-stacking h_π, and the sharp first-order reflection from columnar lattice D_{col} (Fig. 1c). In addition, it presents broad signals at small- and medium-angles testifying of other periodic features; above all, a strong and quite sharp wide-angle reflection h_{ph} evidences the occurrence of a three-dimensional structure of which the columnar lattice is a sub-arrangement. To summarize, in solid state, the PBLC dyes stack on the top of each other to form a 3D columnar mesophase with a rotational displacement of the aromatic cores along the column axis as illustrated in the insert of Fig. 1c. Note that a full resolution of structure and discussion of self-assembly goes beyond the scope of this contribution and will be published separately.

The optical properties of PBLC were investigated by UV/Vis and fluorescence spectroscopy. The absorption spectrum in dichloromethane (DCM) showed a broad S_0 - S_1 band with an absorption maximum wavelength at 577 nm and two other bands at around 539 nm and 449 nm, respectively (Fig. 1d and Fig. S1). The emission spectrum is approximately the mirror image of the S_0 - S_1 absorption band with a maximum wavelength at 616 nm and a Stokes shift of about 39 nm. The PLQYs of PBLC in solution are very high with values of about 90 % and 98 % in DCM and toluene, respectively. Note that the broadening in solution of both absorption and emission spectra in comparison with unsubstituted perylenes is due to the substantial distortion of the aromatic core caused by the presence of the four bay substituents.[41] In solid state, the UV/Vis and fluorescence spectra of PBLC showed only a small bathochromic shift (about 7 nm) and only minor changes in the band shapes upon aggregation (see Fig. S1). Both observations imply that the excitonic couplings between molecules are weak in the room temperature columnar mesophase. In addition, the PLQY is around 30 % which is higher than the typical PLQY values of unsubstituted perylene derivatives in solid state.[35] These results indicate that PBI cores with four bulky phenoxy substituents cannot closely stack due to the steric hindrance in the mesophase. However, these molecules are packed up in the columnar stack with a rotational disorder along the column axes. This description is consistent with the columnar arrangement suggested by the mesophase structure investigation (see above). In addition, it also indicates a random distribution perpendicular to the columnar axis of the transition dipole moments located in the plane of the perylene cores (see inset Fig. 1c).

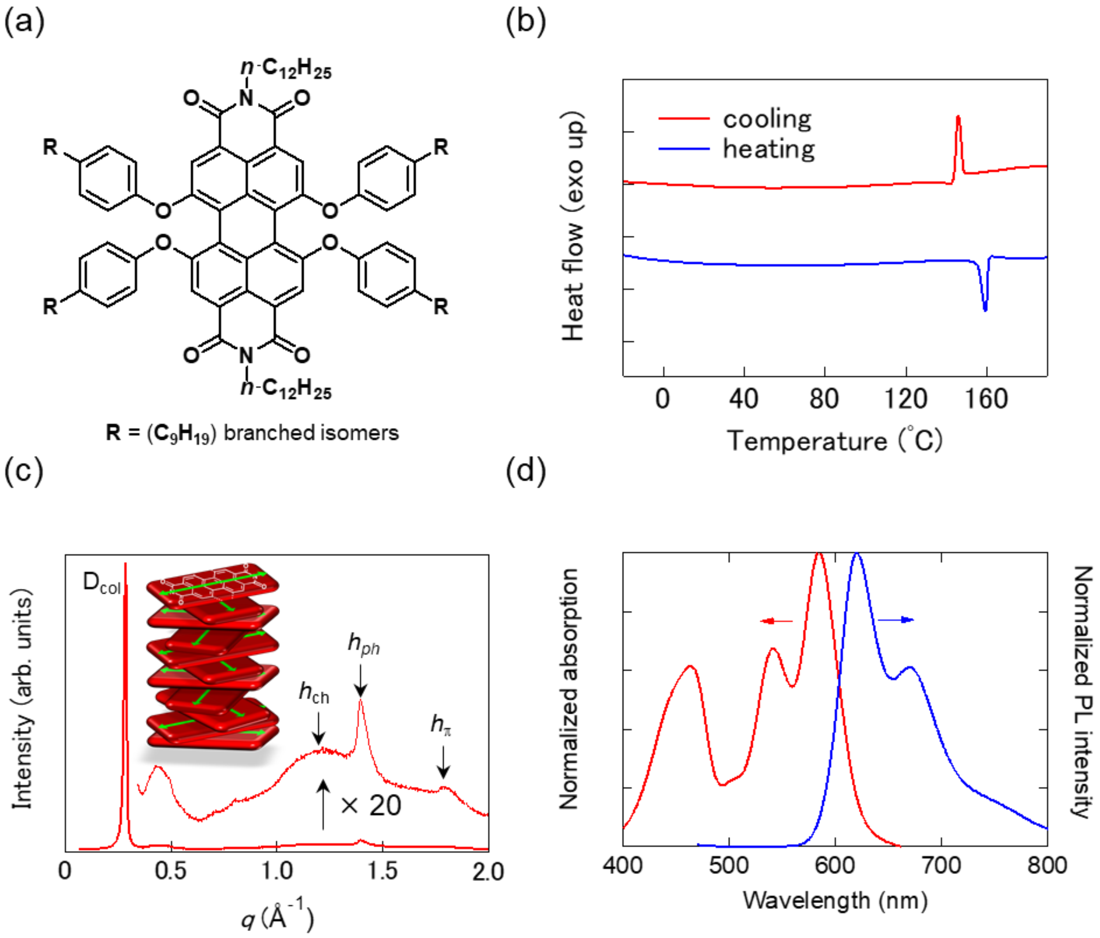

Figure 1. (a) Chemical structure of PBLC. (b) DSC trace of PBLC upon second heating and first cooling cycles at 5 °C/min. (c) SWAXS pattern of PBLC at 20°C with signals h_{ch}, h_{π}, and D_{col} from columnar lattice and h_{ph} from three-dimensional superstructure. (Inset: schematic representation of the molecular packing of perylene cores along of the columnar axis. The double green arrows in the plane of perylene cores represent the direction of the transition dipole moment of perylene dyes) (d) Absorption (red) and photoluminescence (blue) spectra of the spin coated PBLC neat film.

Based on the order and dynamic properties of liquid crystal materials [34], two types of PBLC thin films with large oriented single domains were prepared. These films were fabricated by melt processing between two quartz substrates separated by gold pads with a controlled thickness of 200 nm (**Fig**. 2a).[31] The use of ultra-clean bare or octadecyltrichlorosilane (OTS)-treated quartz substrates leads to the different thin films in which PBLC molecules adopt either homeotropic or planar orientation with a face-on or edge-on orientation of discotic cores, as illustrated in Fig. 2a. The details of the fabrication of the empty quartz cell and the preparation of the oriented thin films are given in supplementary information section 2A. The homeotropic or planar alignments of PBLC molecules were confirmed by POM and grazing-incidence wide-angle X-ray scattering (GIWAXS) measurements. The optical textures observed by microscopy under crossed polarizers for the films prepared with bare or OTS-treated quartz substrates show the typical "black" dendritic or pseudo focal-conic textures of homeotropic and planar orientation, respectively (Supplementary Fig. S3 a and b) [34]. In addition, the GIWAXS patterns of the homeotropic films also evidence the perfect face-on orientation of the discotic molecules with the columns oriented perpendicular to the substrate for non-treated quartz substrates and an orthogonal molecular orientation (columns lain on the substrate) for OTS-treated substrates (Fig. 2b). [42]

Figure 2c shows the extinction coefficient spectrum for the PBLC thin films with homeotropic and planar alignment between quartz substrates. The absorption coefficient of the PBLC homeotropic thin films is nearly twice larger than that with planar orientation (at 580 nm, $A^{\text{homeotropic}}/A^{\text{planar}} \sim 2.0$), which matches well theoretical ratio calculated from the electric field and the orientation of the dipole moments (Supplementary Section 5C). This stronger absorption of homeotropic alignment is consistent with the face-on orientation of the PBLC molecules, leading to a distribution of the transition dipole moments exclusively in the plane of the film.

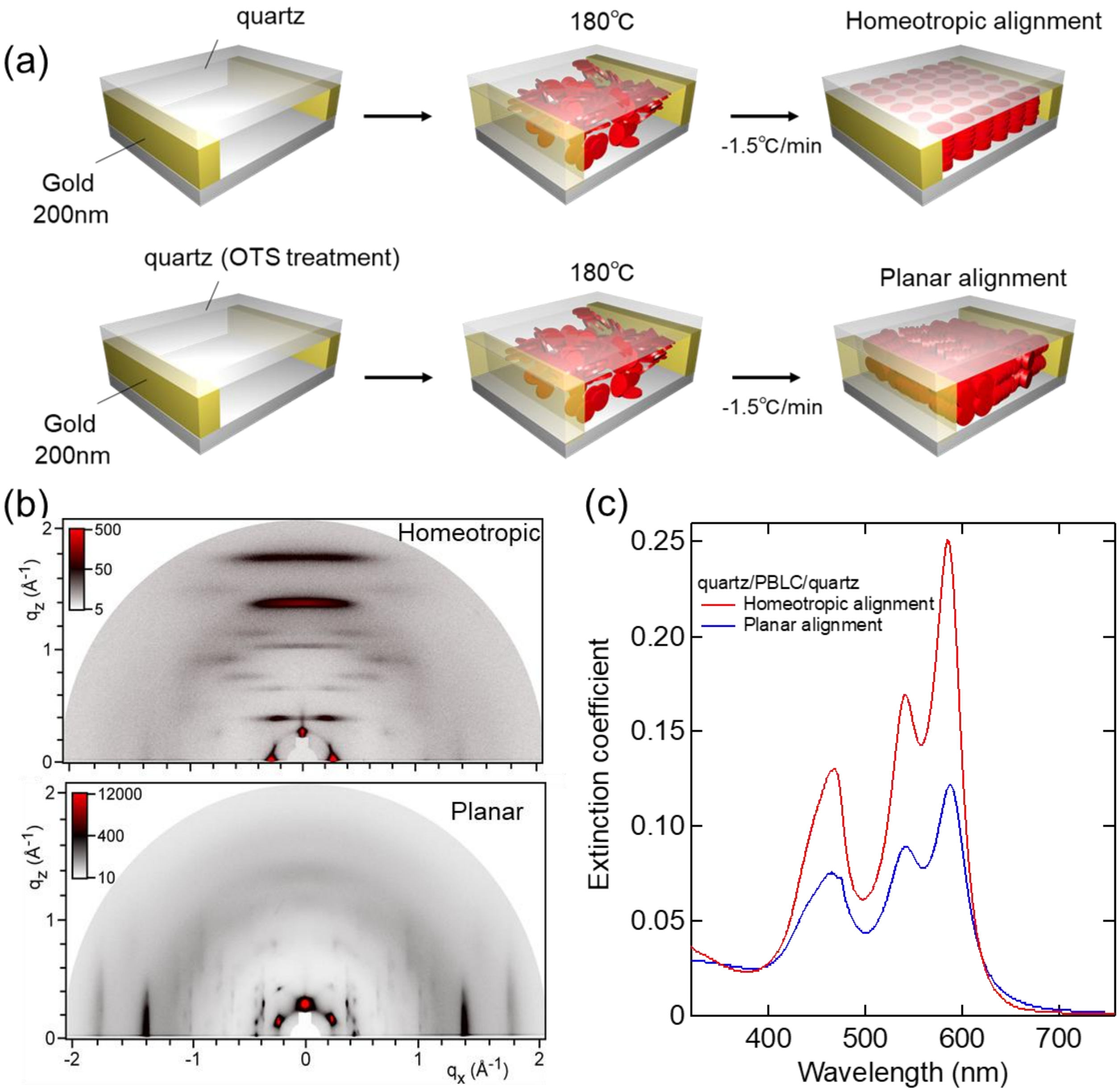

Figure 2. (a) Fabrication method of the melt-grown PBLC thin film sandwiched between two quartz substrates. Homeotropic alignment was obtained using clean SiO_2 substrate. Planar alignment was obtained by using octadecyltrichlorosilane (OTS) treated substrates. (b) GIWAXS characterization for homeotropic and planar alignment (c) Extinction coefficient spectra of homeotropic and planar melt-grown PBLC thin films (200 nm) .

To explore polariton properties of PBLCs, two types of microcavities containing oriented thin films with homeotropic and planar alignment were fabricated according to the procedure described previously (see supplementary Fig. S5a). These two microcavities are composed of a 270 nm thick film of PBLC sandwiched between two dielectric mirrors, which composed of SiO_2/Ta_2O_5 with $\lambda/4$ thickness as displayed in **Fig**. 3. The top mirror of 6 pairs has a reflectivity of 98.4 %, and the bottom mirror of 10 pairs has a reflectivity of 99.88 % in the stopband, respectively. The thickness of the emitter layer was estimated by measuring transmittance of empty DBR/Air/DBR cavity (Supplementary Fig. S6a) and the Q factor for each microcavity is approximately 200 (Supplementary Fig. S6b). The homeotropic and planar alignment of PBCL molecules in the two microcavities were confirmed by POM as shown in Figs. S5b-c. The microcavities containing PBLC with homeotropic and planar alignment will be called hereafter MC-HO and MC-PL, respectively.

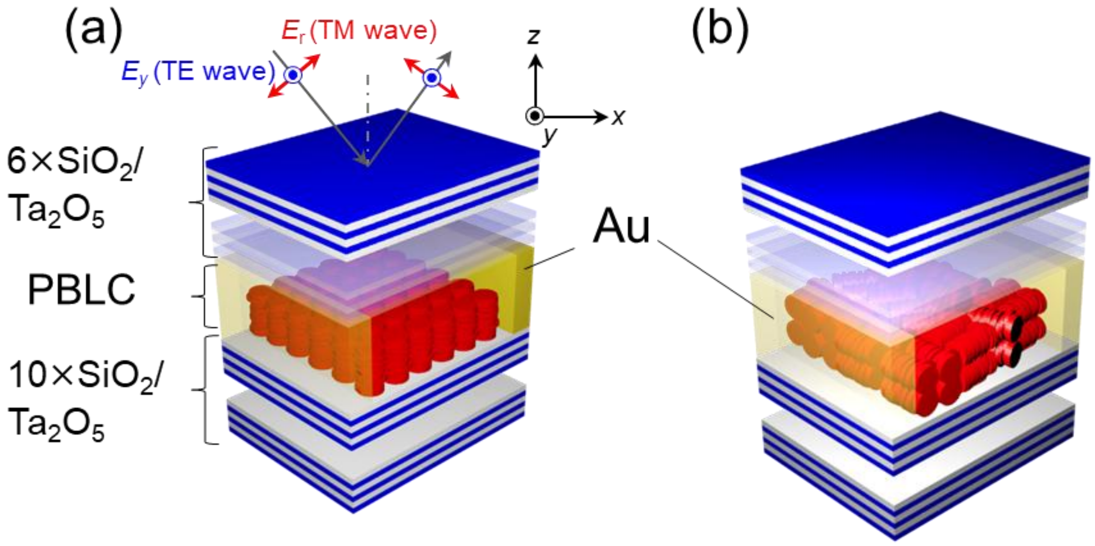

Figure 3. (a) Schematic representation showing the fabricated microcavity structure by melt-grown method, which consists of two dielectric mirrors of alternating tantalum pentoxide (Ta_2O_5) and silicon dioxide (SiO_2) pairs enclosing a single layer of homeotropic and planar aligned PBLC. Planar alignment (right side) was obtained by treating the DBR surface with OTS (please see Fig. S5 (a)). Thickness of PBLC layer is 270 nm for MC-HO and MC-PL. Also, transverse magnetic (TM) polarization is defined when the electric field is parallel to the incident surface (x-z plane), and transverse electric (TE) polarization is defined when the electric field is perpendicular to the incident surface.

Figure 4 shows a contour map of the transverse magnetic (TM) angle resolved reflectivity measured for MC-HO and MC-PL, respectively. The squares show the dip position identified on the reflectance spectrum for each angle (Supplementary Fig. S8). In both MC-HO and MC-PL microcavities, three peaks are found to anticross around vibronic resonances of $E_{ex}^{0\text{-}0}$ = 2.11 eV, $E_{ex}^{0\text{-}1}$ = 2.29eV. These are a characteristic behavior indicating a strong coupling state and associated with the lower polariton (LP), middle polariton (MP) and upper polariton (UP) branches. A contour map of the transverse electric (TE) angle resolved reflectivity for MC-HO and MC-PL are shown in Fig. S9, respectively. In this case, the dip structure derived from the upper and middle polariton was not observed due to the high reflectance of the top mirror.

To estimate the strong coupling parameters for the obtained LP, MP, and UP dispersion curves, we simulated these dispersion curves by a coupled harmonic oscillator Hamiltonian [9]:

$$\begin{pmatrix} E_{ph} & V_1 & V_2 \\ V_1 & E_{ex}^{0-0} & 0 \\ V_2 & 0 & E_{ex}^{0-1} \end{pmatrix}\begin{pmatrix} \alpha \\ \beta \\ \chi \end{pmatrix} = E\begin{pmatrix} \alpha \\ \beta \\ \chi \end{pmatrix} \#(\text{Erreur ! Signet non défini.})$$

where V_1, V_2 are interaction potentials, $E_{\mathrm{ex}}{}^{0\text{-}0} = 2.11$ eV, $E_{\mathrm{ex}}{}^{0\text{-}1} = 2.29$ eV are uncoupled exciton energies and $\{|\alpha|^2\}$, $\{|\beta|^2, |\chi|^2\}$ is the Hopfield coefficient of the photonic and excitonic components. The cavity photon dispersion is given by

$$E_{\mathrm{ph}}(\theta) = E_{\mathrm{ph}}(0)\left(1 - \frac{\sin^2\theta}{n_{\mathrm{eff}}}\right)^{-1/2} \#(\text{Erreur ! Signet non défini.})$$

The solid black lines in Fig. 4 trace the fit dispersion of the LP, MP and UP branches. The dashed black line shows the dispersion of the uncoupled exciton ($E_{\mathrm{ex}}{}^{0\text{-}0}$, $E_{\mathrm{ex}}{}^{0\text{-}1}$) and cavity photon obtained from simulation. The resulting fit parameters are shown in Fig. 4. Using the interaction potential, V_1, obtained from the fit, the Rabi splitting between LP and MP for MC-HO and MC-PL are $\hbar\Omega_{HO}^{TM} = 160 \pm 5$ meV and $\hbar\Omega_{PL}^{TM} = 120 \pm 5$ meV. This is a consequence of the anisotropic behavior with respect to the orientation of the PBLC column. The photonic $\{|\alpha|^2\}$ and excitonic $\{|\beta|^2, |\chi|^2\}$ weights for each branch are shown in insets of Fig. 4. The Rabi splittings for TE polarization were estimated to be $\hbar\Omega_{HO}^{TE} = 180 \pm 5$ meV and $\hbar\Omega_{PL}^{TE} = 125 \pm 5$ meV for MC-HO and MC-PL, respectively.

Here, we discuss the polarization dependence of the Rabi splitting in the MC-HO and MC-PL microcavities. From the Tavis-Cumming model, which describes a single cavity mode interacting with *N* dipoles, the Rabi splitting energy $\hbar\Omega$ is given as

$$\hbar\boldsymbol{\Omega} = \sqrt{\frac{2|\boldsymbol{\mu}\cdot\boldsymbol{n}|^2\boldsymbol{\omega}(\boldsymbol{N}/\boldsymbol{V_0})}{\boldsymbol{\varepsilon}}} \#(\text{Erreur ! Signet non défini.})$$

where ε and V_0 are the dielectric constant and cavity volume, respectively.[2] ω is the angular frequency of the electric field $\boldsymbol{E}$ and $\boldsymbol{n}$ is a unit vector pointing in the direction of the electric field. From equation (3), the Rabi splitting is largest when the direction of the electric field is parallel to the dipole moment ($\boldsymbol{\mu}$ // $\boldsymbol{n}$). For MC-HO, the Rabi splitting for the TE polarization has a larger value compared with that of the TM mode ($\hbar\Omega_{HO}^{TE} = 180 \pm 5\, meV > \hbar\Omega_{HO}^{TM} = 160 \pm 5$ meV) because the dipole moment of the PBLC with a homeotropic alignment is directed in-plane (parallel to the substrate). On the other hand, for MC-PL, the Rabi splitting energies for the TE and TM mode have almost equal values ($\hbar\Omega_{PL}^{TE} = 125 \pm 5$ meV ~ $\hbar\Omega_{PL}^{TM} = 120 \pm 5$ meV) because the dipole moment of PBLC is isotopically oriented.

The difference of the Rabi splitting between MC-HO and MC-PL can be explained by the anisotropy of the absorption of the PBLC for each alignment. The transition dipole moment is related to the absorption by $N\mu^2 \propto Nf \propto \int \alpha(\omega)\mathrm{d}\,\omega$, where μ is transition dipole moment, f is oscillator strength and $\alpha(\omega)$ is absorption coefficient. Thus, the vacuum Rabi splitting is proportional to the square root of the absorption spectrum ($\hbar\Omega \propto \sqrt{\int \alpha(\omega)\mathrm{d}\omega}$). The ratio of Rabi splitting energy between MC-HO and MC-PL is $\hbar\Omega_{HO}^{TM}/\hbar\Omega_{PL}^{TM} = 1.33$ $\left(\hbar\Omega_{HO}^{TE}/\hbar\Omega_{PL}^{TE} = 1.44\right)$. On the other hand, the square root of the ratio of the absorption coefficient of PBLC with homeotropic and planar alignment is $\sqrt{A^{\mathrm{HO}}/A^{\mathrm{PL}}} = \sqrt{2} = 1.44$, which is comparable to the ratio of Rabi splitting. These results indicate that the difference in Rabi splitting between MC-HO and MC-PL originates from the difference of orientations of PBLC columns

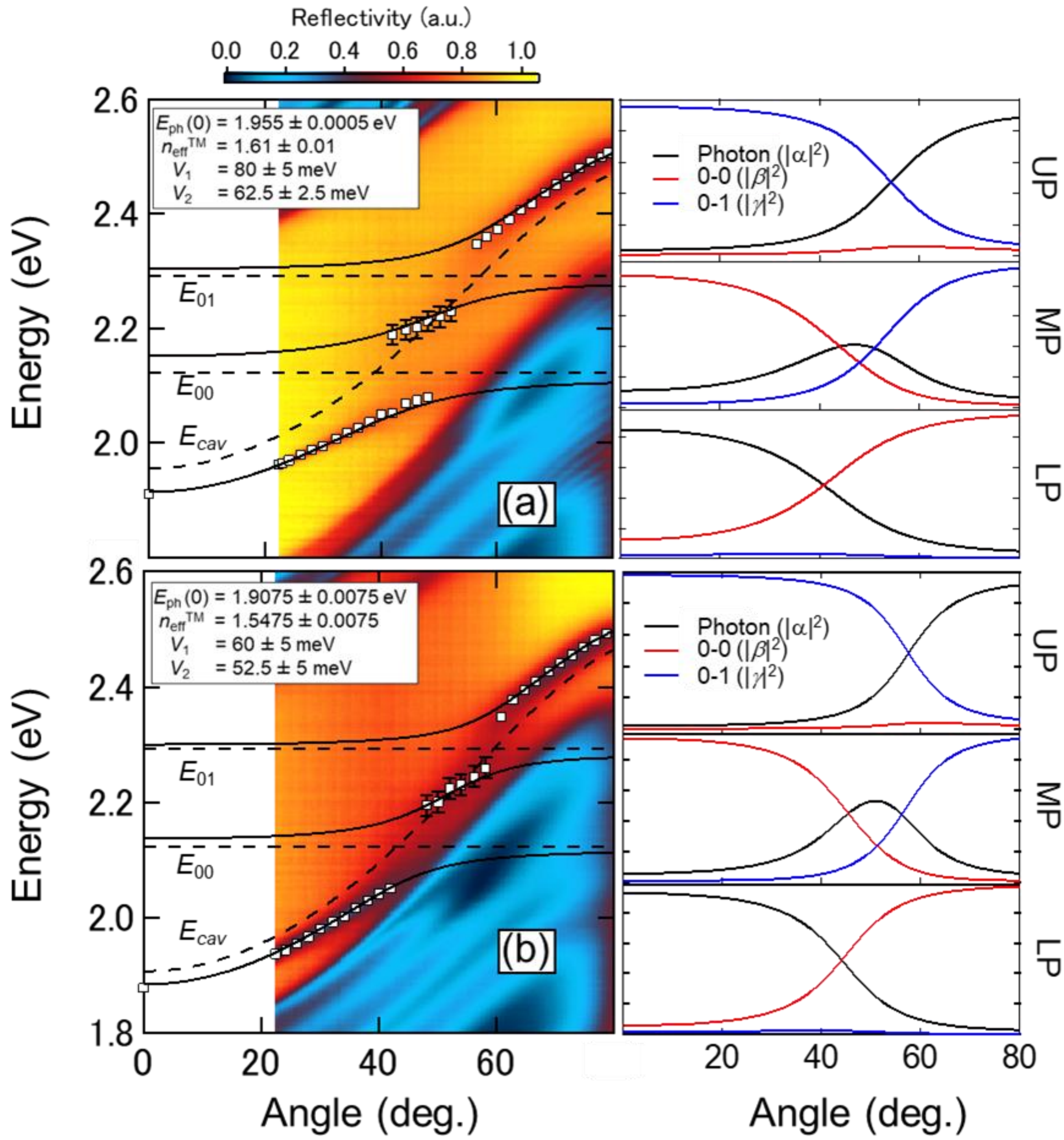

Figure 4. Left : Contour maps of the angle-resolved reflectivity for transverse magnetic polarization for MC-HO and MC-PL. The position of individual minima identified on the spectra are shown as white squares dots for each angle (see Fig. S8). The black solid lines are a fit to a 3-body coupled harmonic oscillator Hamiltonian (CHO). Also, the dashed black line shows the dispersion of the uncoupled exciton ($E_{ex}^{0\text{-}0}$ = 2.11 eV , $E_{ex}^{0\text{-}1}$ = 2.29 eV) and cavity photon dispersion obtained from CHO, Right : Photonic and excitonic branch content for each polariton branch (TM mode). These data are shown for MC-HO and MC-PL in (a) and (b), respectively.

To investigate the polariton population distribution, angle-resolved PL for TM polarization was measured for MC-HO and MC-PL with a detection cone of half angle $\theta = 4$ deg. The microcavities were pumped non-resonantly, at $\theta = 50$ deg, using 7 ns pulses from a $\lambda = 337$ nm N_2 laser (see method for details). The behaviors of angle-resolved PL coincide with the dashed white lines in **Fig. 5** showing the position of LP obtained from angle resolved reflectance measurements, suggesting that the PL originates from radiation of lower polariton. From the measured PL linewidth for MC-HO and MC-PL, the lower polariton lifetimes are estimated to be $\tau_{\mathrm{LP}}{}^{\mathrm{HO}}$ ~ 58.3 fs, $\tau_{\mathrm{LP}}{}^{\mathrm{PL}}$ ~ 51.4 fs, respectively.

The PL intensity can be related to the number of polaritons at a given energy and angle, and the corresponding polariton lifetime. Under non-resonant excitation, the dark exciton reservoir is first populated. In the case where exciton-phonon coupling is weak, two scattering mechanisms have been proposed to explain the subsequent relaxation to the lower polariton branch. As discussed in Ref. 18 and 21, this can occur radiatively through the emission of a photon at the energy of one of the vibronic replicas, or non-radiatively through the emission of a molecular vibration from the excited state. The balance between the 2 processes is determined by $\frac{W_{\mathrm{RAD}}}{W_{\mathrm{NON-RAD}}} \propto |\alpha|^2/|\beta|^2$, where W_{RAD} and $W_{\mathrm{NON\text{-}RAD}}$ are the rates corresponding to radiative and non-radiative scattering, respectively, while $|\alpha|^2$ and $|\beta|^2$ are the photonic and excitonic Hopfield coefficients, respectively. In our case, $|\alpha|^2/|\beta|^2 > 1$ in the range of 0 deg to 35 deg for MC-HO and MC-PL, respectively ($W_{\mathrm{rad}}/ W_{\mathrm{non\text{-}rad}} > 1$) (Fig. 5 inset). This suggests that radiative pumping should be the main source of relaxation to the LP branch. In addition, the PL intensity for MC-PL and MC-HO is strongest at $\theta =$ 0 deg and decrease monotonically with increasing of angle, indicating the absence of a relaxation bottleneck. [44]

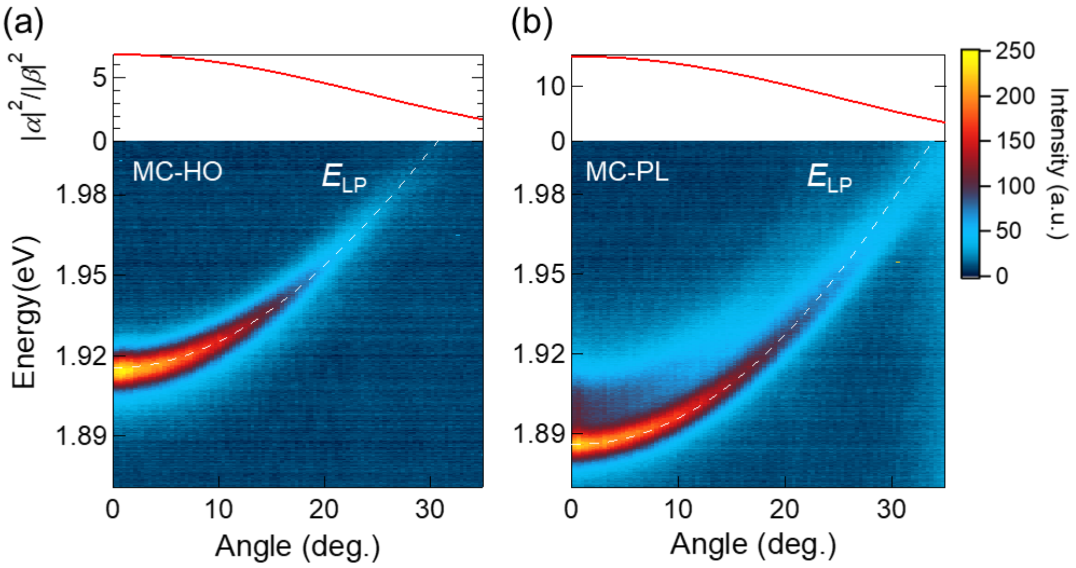

Figure 5. Bottom: Transverse-magnetic-polarized photoluminesence for (a) MC-HO and (b) MC-PL microcavities under 377nm excitation showing exciton-polariton emission from the LP branch. The white dashed line shows the position of lower polariton obtained from the angle-resolved reflectivity. Top: $|\alpha|^2/|\beta|^2$ show the rate of exciton and photon Hopfield coefficient. Effective polariton relaxation determined by radiative and non-radiative channels depends on $|\alpha|^2/|\beta|^2$.

The emission lifetime from the lower polariton level was measured using a streak camera with a detection cone of half angle $\theta = 5$deg (**Fig**. 6). The microcavities were pumped non-resonantly, at $\theta = 45$ deg, using a Ti:Sapphire regenerative amplifier with a pulse width of 120 fs, a wavelength $\lambda = 400$ nm, a repetition rate of 1kHz (see method for details). The excitation intensity was adjusted so that the absorbed pump fluence is 1.0 μJcm^{-2}. At this excited energy regime, the emission follows single-exponential decay in the MC-HO and MC-PL, with $\tau^{\text{MC-HO}} = 3.8$ ns, $\tau^{\text{MC-PL}} = 4.2$ ns, respectively. The lifetime of PBLC outside the cavity is $\tau_0 = 5.0$ ns for the homeotropic and planar alignment. As can be seen from these values, the lifetime inside the cavity is shorter than that of outside the cavity. This behavior can be caused by the increased radiative decay rate due to a modification of the photon mode density in the microcavities, the so-called Purcell effect, and an enhanced scattering of the exciton reservoir to the lower polariton level.

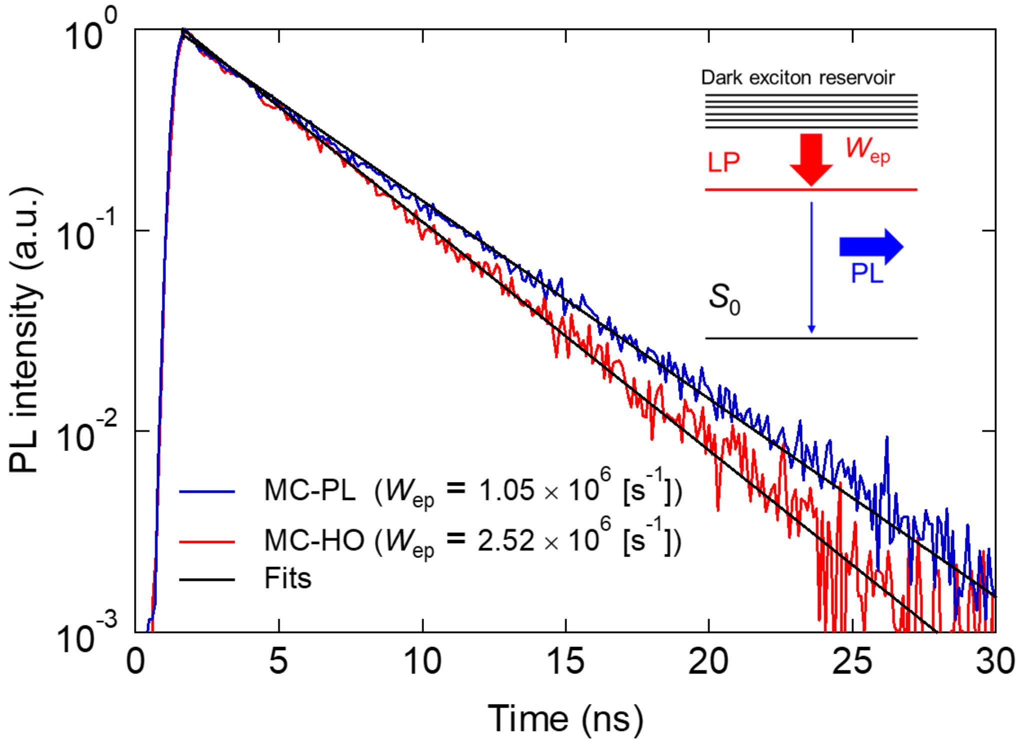

Figure 6. The time-resolved lower polariton emission for MC-HO and MC-PL under 400nm excitation. The excitation intensity was adjusted so that the absorbed pump fluence was 1.0 μJcm^{-2}. At this excited energy regime, the emission follows single-exponential decay in the MC-HO and MC-PL, with $\tau^{\text{MC-HO}}$ = 3.8 ns, $\tau^{\text{MC-PL}}$ = 4.2 ns, respectively. Also, the dashed black lines show the results of single exponential fittings. From these lifetimes and the photoluminescence quantum yields (PLQY) of the lower polaritons, the polariton relaxation efficiency were estimated to be $W_{ep}{}^{\text{HO}} \sim 2.52 \times 10^6$ [s^{-1}], $W_{ep}{}^{\text{PL}} \sim 1.05 \times 10^6$ [s^{-1}] for MC-HO and MC-PL, respectively. (Inset : Schematic illustration of polariton relaxation.)

To discuss the modified radiative decay rate inside the cavity, we estimated the radiative decay rate inside the cavity normalized by the damping rate in the absence of a local structure (see Supplementary section 5A, B). The values of the normalized damping rate were estimated to be $F_p{}^{\text{MC-HO}}$ = 1.04 and $F_p{}^{\text{MC-PL}}$ = 1.03 for MC-HO and MC-PL, respectively. On the other hand, experimentally observed normalized damping rate is $\tau_0/\tau^{\text{MC-HO}}$ = 1.32 and $\tau_0/\tau^{\text{MC-PL}}$ = 1.19, where τ_0 is the lifetime of PBLC outside the cavity. This difference between the calculation and experimental values shows that these reduced lifetimes cannot be completely explained by the Purcell effect.

To understand this effect, we modelled the dynamics of the polariton relaxation using a minimal rate-equation approach. From the discussion of the angle-resolved PL measurement results, we find that the macroscopic dynamics resulting in the polariton relaxation process is that of a two-level process rather than that of the polariton bottleneck. Therefore, we consider a two-level master equation for dark excitons in the reservoir and the ensemble of lower polaritons.

$$\frac{\mathrm{d}[\boldsymbol{DS}]}{\mathrm{d}\boldsymbol{t}} = -\left(\boldsymbol{k}_{\boldsymbol{rad}}^{\boldsymbol{DS}} + \boldsymbol{k}_{\boldsymbol{nr}} + \boldsymbol{W}_{\boldsymbol{ep}}\right)[\boldsymbol{DS}] - \boldsymbol{\gamma}[\boldsymbol{DS}]^2 \#(\mathbf{4})$$

$$\frac{\mathrm{d}[\boldsymbol{LP}]}{\mathrm{d}\boldsymbol{t}} = \boldsymbol{W}_{\mathrm{ep}}[\boldsymbol{DS}] - \frac{[\boldsymbol{LP}]}{\boldsymbol{\tau}_{\boldsymbol{LP}}} \#(\mathbf{5})$$

where $[LP]$ and $[DS]$ are the surface density of lower polariton and the reservoir of dark excitons, respectively. k_{rad}^{DS} (k_{nr}) is the radiative decay rate (the non-radiative decay rate, resp.) of the reservoir of dark excitons. W_{ep} is the rate of resonant excitation transfer from exciton reservoir to lower polariton, γ is the bimolecular annihilation rate, and $\tau_{LP}$is the lifetime of lower polaritons. Note that we ignore bimolecular quenching of polaritons because [LP] is much smaller than [DS]. When the bimolecular annihilation rate is sufficiently small, the solutions of Eq. (4) and (5) is $[DS] = n_{e0}e^{-\Gamma_0 t}$, where n_{e0} is an exciton density at time t = 0 and Γ_0 is a total decay rate, $\Gamma_0 = k_{rad}^{DS} + k_{nr} + W_{ep}$. The photoluminescence quantum yield (PLQY) of lower polaritons, Φ_{LP}, can be written as $\Phi_{LP} = W_{ep}/(k_{rad}^{DS} + k_{nr} + W_{ep})$. The result is that the polariton relaxation rate can be calculated from PLQY of a lower polaritons and a total decay rate, $W_{ep} = \Phi_{LP}\Gamma_0$.

To determine the polariton relaxation rate, W_{ep}, the PLQY of the LPs was measured.[43] In this approach, PLQY (Φ_{PL}) is given by $\Phi_{LP} = \int I_{LP}(\lambda)d\lambda/\int(I_{int}(\lambda) - I'_{int}(\lambda))d\lambda$, where $I_{\mathrm{LP}}(\lambda)$ is the emission spectrum of the lower polaritons over all angles, $I_{int}(\lambda)$ $(I'_{int}(\lambda))$ is the excitation light spectrum in the absence of the sample (in the presence of the sample, resp.). In this notation, $\int(I_{int}(\lambda) - I'_{int}(\lambda))d\lambda$ corresponds to the number of absorbed photons from the excitation light. Fig S12 shows the PL spectrum of MC-HO and MC-PL upon excitation at 400 nm. The sharp lines to the left are the excitation profiles $I_{int}(\lambda)$ and $I'_{int}(\lambda)$. $I_{\mathrm{LP}}(\lambda)$ was extracted by separating the PL spectrum of MC-HO and MC-PL from that of PBLC. For fitting, the LP spectrum was taken to be an asymmetric Gaussian distribution (Supplementary section 5C). These parameters were shown in

Table S3. As a result, the LP PLQY is estimated to be $\Phi_{\mathrm{LP}}^{HO} = 0.96 \pm 0.20$ % and $\Phi_{\mathrm{LP}}^{PL} = 0.43 \pm 0.15$ % for MC-HO and MC-PL, respectively. Meanwhile, the total decay rates of Γ_0 are given by $\Gamma_0 = \frac{1}{\tau^{MC-HO}} = 2.63 \times 10^8\ [s^{-1}]$ and $\Gamma_0 = \frac{1}{\tau^{MC-PL}} = 2.38 \times 10^8\ [s^{-1}]$ for MC-HO and MC-PL, respectively. Therefore, the polariton relaxation efficiencies were calculated to be $W_{\mathrm{ep}}^{\mathrm{HO}} = 2.5 \pm 0.5 \times 10^6\ [\mathrm{s}^{-1}]$ and $W_{\mathrm{ep}}^{\mathrm{PL}} = 1.0 \pm 0.3 \times 10^6\ [\mathrm{s}^{-1}]$ for MC-HO and MC-PL, indicating that the polariton relaxation rate of MC-HO is twice as fast as that of MC-PL.

To discuss this difference in polariton relaxation efficiencies, we calculated the relaxation rate based on a microscopic model for radiative scattering from the dark states to the LP.[18] In this case, the relaxation rate to LPs in the spectral interval $[E_{inf}, E_{sup}]$ is given by

$$\boldsymbol{W_{\mathrm{ep}} = \frac{\pi S|\alpha|^2}{2} \frac{m_{LP} V_1^2}{\overline{\nu}_{\mathrm{e}} \hbar^3} \int_{E_{\mathrm{inf}}^{\mathrm{A0}}}^{E_{\mathrm{sup}}^{\mathrm{A0}}} f\left(E_{\mathrm{inf}}^{\mathrm{A0}} - E\right) \mathrm{d}E \ \#(6)}$$

where S is the Huang-Rhys parameter and $|\alpha|^2$ is the photonic coefficient at $k_{||} = 0$ and m_{LP} is the effective mass of LP obtained from dispersion relationship, $m_{LP}^{-1} = \hbar^{-1}\left(\mathrm{d}^2 E_{\mathrm{LP}}/\mathrm{d}k_{||}^2\right)$, V_1 is the coupling constant and $\overline{\nu}_{\mathrm{e}} = 1.01 \times 10^{16}$ [cm^{-2}] is the surface density of excitons.[45] $f(E)$ is a function of the normalized line shape of the (0-1) PL peaks. In this work, we consider a normalized Gaussian distribution (Supplementary Fig. S14). Moreover, $[E_{\mathrm{inf}}, E_{\mathrm{sup}}]$ coincides with the LP energy region measured in PLQY and was estimated to be $E_{\mathrm{inf}}(\theta = 0\ \mathrm{deg}) = 1.8432\ \mathrm{eV}$, $E_{\mathrm{sup}}(\theta = 90\ \mathrm{deg}) = 2.1264\ \mathrm{eV}$ for MC-HO and $E_{\mathrm{inf}}(\theta = 0\ \mathrm{deg}) = 1.8288\ \mathrm{eV}$, $E_{\mathrm{sup}}(\theta = 90\ \mathrm{deg}) = 2.1216\ \mathrm{eV}$ for MC-PL. Based on these previous parameters (Table 1), the polariton relaxation rates were calculated to be $W_{\mathrm{ep}}^{\mathrm{HO}} = 2.54 \times 10^6\ [\mathrm{s}^{-1}]$ and $W_{\mathrm{ep}}^{\mathrm{PL}} = 1.57 \times 10^6\ [\mathrm{s}^{-1}]$ for MC-HO and MC-PL, respectively. This difference in the polariton relaxation efficiencies is mostly derived from the coupling constant V_1. This result shows that the acceleration of the polariton relaxation rate was caused by the control of the dipole moment of PBLC. These results show that the alignment of the dipole moments is an important factor for the accelerating polariton relaxation.

Table 1. Parameters for the calculation of polariton relaxation efficiency

Cavity name	S a)	m_{LP} b) [kg]	$\bar{\upsilon}_e$ c) [cm^{-2}]	V_1 d) [meV]	$\int f(E)dE$ e)	W_{ep}^{cal} f) [s^{-1}]	W_{ep}^{ex} f) [s^{-1}]
MC-HO	0.6	$4.49 \times 10^{-6} m_0$	1.01×10^{16}	80 ± 10	0.56	2.54×10^{6}	2.52×10^{6}
MC-PL	0.6	$4.03 \times 10^{-6} m_0$	1.01×10^{16}	60 ± 2.5	0.63	1.57×10^{6}	1.05×10^{6}

a) Huang Rhys parameter; b) the effective mass of lower polariton and m_0 is electron mass ($m_0 = 9.1 \times 10^{-31}$ kg); c) surface density of excitons, calculated from molecular density of PBLC; d) coupling constant; e) integral of the normalized line shape of the (0-1) photoluminescence; f) calculated polariton relaxation efficiency and experimentally obtained polariton relaxation efficiency

Conclusion

In summary, we prepared organic microcavities based on well oriented thin films of a liquid crystalline perylene semiconductor, presenting either a face-on or edge-on molecular orientation between two dielectric mirrors. The results clearly evidenced that the face-on orientation of the perylene dyes enhances not only the Rabi splitting but also the polariton relaxation efficiency in the optical cavity. These outcomes show that the in-plane orientation of dipole moments is a promising strategy for lowering the BEC threshold mainly related to the polariton relaxation rate. They also demonstrate that self-organized semiconducting materials such as liquid crystalline semiconductors are interesting candidates for low threshold polariton BEC. Combined with their typical high charge carrier mobility, such derivatives are also promising candidates for possible low power electrically driven polariton devices.

Experimental Methods

Angle resolved photoluminecence measurements: Photoluminescence was measured using a spectrometer fibre-coupled to a computer-controlled goniometer. The detection half-angle of collection lens is $\Delta\theta = 4°$. The microcavities were pumped non-resonantly, at $\theta = 50°$, using 7 ns pulses from a $\lambda = 337$ nm N_2 laser in the scan range of 0° to 45° to prevent the detection of the scattered light of the laser excitation in the high angle region. In addition, the N_2 laser was used to prevent sample degradation during the measurements. The use of the laser enables stable angle-resolved PL measurement without a decrease of PL due to the degradation.

Time resolved photoluminecence measurements: Time-resolved photoluminescence (TR-PL) measurements were performed using a streak camera (Hamamatsu C4334) coupled to the regenerative Ti:Sapphire amplifier (Spitfire Ace, ~120 fs, 1 kHz, 4 mJ pulse^{-1} , 800 nm). The samples were pumped non-resonantly at incident angle $\theta = 45°$ by the second harmonic (SH) of a fundamental pulse from the amplifier. The incident angle of the excitation light was fixed at 45° to increase the exciton efficiency at $\lambda = 400$ nm. Time resolution of the total detection system was ~ 30 ps. Detection angle was + 5° from normal direction to the microcavity.

・Acknowledgement

We thank Pohang Accelerator Laboratory (PAL) for giving us the opportunity to perform the GIWAXS measurements, MEST and POSTECH for supporting these experiments, Dr. Hyungju Ahn for adjustments and help, and other colleagues from the 9A USAXS beamline for assistance. Part of this work was also supported by the CNRS (PICS N° 8085), France. This work was partially supported by JSPS KAKENHI Grant Numbers JP17H06375 and JP20H05106, JSPS Core to Core program.

Received: ((will be filled in by the editorial staff))
Revised: ((will be filled in by the editorial staff))
Published online: ((will be filled in by the editorial staff))

References

[1] A. Kavokin, J. Baumberg, G. Malpuech, F. P. Laussy, *Microcavities*, Oxford University Press, Oxford, **2008**.

[2] M. Fox, *Quantum Optics*, Oxford University Press, Oxford, **2006**.

[3] H. Deng, G. Weihs, D. Snoke, J. Bloch, Y. Yamamoto, *PNAS, Proc. Natl. Acad. Sci. USA* **2003**, *100*, 15318.

[4] T. C. Lu, Y. Y. Lai, Y. P. Lan, S. W. Huang, J. R. Chen, Y. C. Wu, W. F. Hsieh, H. Deng, *Opt. Express* **2012**, *20,* 5530.

[5] F. Li, L. Orosz, O. Kamoun, S. Bouchoule, C. Brimont, P. Disseix, T. Guillet, X. Lafosse, M. Leroux, J. Leymarie, M. Mexis, M. Mihailovic, G. Patriarche, F. Réveret, D. Solnyshkov, J. Zuniga-Perez, G. Malpuech, *Phys. Rev. Lett.* **2013**, *110*, 196406.

[6] K. S. Daskalakis, P. S. Eldridge, G. Christmann, E. Trichas, R. Murray, E. Iliopoulos, E. Monroy, N. T. Pelekanos, J. J. Baumberg, P. G. Savvidis, *Appl. Phys. Lett.* **2013**, *102*, 101113.

[7] S. Christopoulos, G. Baldassarri Höger von Högersthal, A. J. D. Grundy, P. G. Lagoudakis, A. V. Kavokin, J. J. Baumberg, G. Christmann, R. Butté, E. Feltin, J.-F. Carlin, N. Grandjean, *Phys. Rev. Lett.* **2007**, *98*, 126405.

[8] D. G. Lidzey, D. D. C. Bradley, M. S. Skolnick, T. Virgili, S. Walker, D. M. Whittaker, *Nature* **1998**, *395*, 53.

[9] D. G. Lidzey, D. D. C. Bradley, A. Armitage, S. Walker, M. S. Skolnick, *Science* **2000**, *288*, 1620.

[10] S. Kéna-Cohen, M. Davanço, S. R. Forrest, *Phys. Rev. Lett.* **2008**, *101*, 116401.

[11] S. Kéna-Cohen, S. A. Maier, D. D. C. Bradley, *Adv. Opt. Mater.* **2013**, *1*, 827.

[12] S. Kéna-Cohen, S. R. Forrest, *Nature Photon*. **2010**, *4*, 371.

[13] J. D. Plumhof, T. Stöferle, L. Mai, U. Scherf, R. F. Mahrt, *Nature Mater*. **2014**, *13*, 247.

[14] K. S. Daskalakis, S. A. Maier, R. Murray, S. Kéna-Cohen, *Nature Mater*. **2014**, *13*, 271.

[15] S. K. Rajendran, M. Wei, H. Ohadi, A. Ruseckas, G. A. Turnbull, I. D. W. Samuel, *Adv. Opt. Mater.* **2019**, ***7***, 1801791.

[16] T. Cookson, K. Georgiou, A. Zasedatelev, R. T. Grant, T. Virgili, M. Cavazzini, F. Galeotti, C. Clark, N. G. Berloff, D. G. Lidzey, P. G. Lagoudakis, *Adv. Opt. Mater.* **2017**, *5*, 1700203.

[17] A. Graf, M. Held, Y. Zakharko, L. Tropf, M. C. Gather, J. Zaumseil, *Nature Mater*. **2017**, *16*, 911.

[18] L. Mazza, S. Kéna-Cohen, P. Michetti, G. C. La Rocca, *Phys. Rev. B* **2013**, *88*, 075321.

[19] D. M. Coles, P. Michetti, C. Clark, W. C. Tsoi, A. M. Adawi, J. S. Kim, D. G. Lidzey, *Adv. Funct. Mater.* **2011**, 21, 3691.

[20] L. Mazza, L. Fontanesi, G. C. La Rocca, *Phys. Rev. B* **2009**, *80*, 235314.

[21] M.Litinskaya, P.Reineker, V.M.Agranovich, *J. Lumin.* **2004**, *110*, 364.

[22] M. Hertzog, M. Wang, J. Mony, K. Börjesson, *Chem. Soc. Rev.* **2019**, *48*, 973.

[23] K. B. Arnardottir, A. J. Moilanen, A. Strashko, P. Törmä, J. Keeling, *Phys. Rev. Lett.* **2020**, *125*, 233603.

[24] K. Goto, K. Yamashita, H. Yanagi, T. Yamao, S. Hotta, *Appl. Phys. Lett.* **2016**, *109*, 061101.

[25] H. Yanagi, F. Sasaki, K. Yamashita, *Adv. Opt. Mater.* **2019**, *7*, 1900136.

[26] W. Gao, X. Li, M. Bamba, J. Kono, *Nature Photon*. **2018**, *12*, 362.

[27] F. L. Roux, R. A. Taylor, D. D. C. Bradley, *ACS Photonics* **2020**, **7**, 746.

[28] F. Le Roux, D. D. C. Bradley, *Phys. Rev. B* **2018**, *98*, 195306.

[29] M. Funahashi, A. Sonoda, *J. Mater. Chem.* **2012**, *22*, 25190.

[30] M. Funahashi, A. Sonoda, *Org. Electron.* **2012**, *13*, 1633.

[31] J. C. Ribierre, Z. Li, X. Liu, E. Lacaze, B. Heinrich, Stephane Méry, P. Sleczkowski, Y. Xiao, F. Lafolet, D. Hashizume, T. Aoyama, M. Uchiyama, J. W. Wu, E. Zaborova, F. Fages, A. D'. Aléo, F. Mathevet, C. Adachi, *J. Mater. Chem. C* **2019**, *7*, 3190.

[32] N. Kani, M. Suzuki, K. Nishiyama, S. Nakanishi, M. Funahashi, N. Tsurumachi, *Phys. Rev. E* **2019**, *100*, 032701.

[33] T. Sakata, M. Suzuki, T. Yamamoto, S. Nakanishi, M. Funahashi, and N. Tsurumachi, *Phys. Rev. E* **2017**, *96*, 042704.

[34] S. Sergeyev, W. Pisulab, Y. H. Geerts, *Chem. Soc. Rev.* **2007**, *36*, 1902.

[35] F. Würthner, C. R. Saha-Möller, B. Fimmel, S. Ogi, P. Leowanawat, D. Schmidt, *Chem. Rev.* **2016**, *116*, 962.

[36] M. Hertzog, P. Rudquist, J. A. Hutchison, J. George, T. W. Ebbesen, K. Börjesson, *Chem. Eur. J.* **2017**, *23*, 18166.

[37] J. A. M. Lugger, D. J. Mulder, S. Bhattacharjee, R. P. Sijbesma, *ACS Nano* **2018**, *12*, 6714.

[38] H. Ocak, B. Bilgin-Eran, M. Prehm, S. Schymura, J. P. F. Lagerwall, C. Tschierske, *Soft Matter* **2011**, *7*, 8266.

[39] S. Kumar, S. K. Varshney, *Angew. Chem. Int. Ed.* **2000**, *39*, 3140.

[40] C. Menelaou, J. ter Schiphorst, A. M. Kendhale, P. Parkinson, M. G. Debije, A. P. H. J. Schenning, L. M. Herz, *J. Phys. Chem. Lett.* **2015**, *6*, 1170.

[41] Z. Chen, U. Baumeister, C. Tschierske, F. Würthner, *Chem. Eur. J.* **2007**, *13*, 450.

[42] A. Gujral, J. Gómez, S. Ruan, M. F. Toney, H. Bock, L. Yu, M. D. Ediger, *Chem. Mater.* **2017,** *29*, 9110.

[43] L.-O. Pålsson, A. P. Monkman, *Adv. Mater.* **2002**, *14*, 757.

[44] H. Deng, H. Haug, Y. Yamamoto, *Rev. Mod. Phys.* **2010**, *82*, 1489.

[45] M. Zhu, Y. Chen, H. Guo, F. Yang, X. Songa, *New J. Chem.* **2018**, *42*, 8998.

[46] F. Lincker, A. Attias, F. Mathevet, B. Heinrich, B. Donnio, J. Fave, P. Rannoua, R. Demadrille, *Chem. Commun.* **2012**, *48*, 3209.

[47] A. Ito, T. Yasuda, X. Ma, M. Watanabe, *Porym J* **2017**, *49*, 31.

[48] L. Mazur, A. Castiglione, K. Ocytko, F. Kameche, R. Macabies, A. Ainsebaa, D. Kreher, B. Heinrich, B. Donnio, S. Sanaur, E. Lacaze, J. Fave, K. Matczyszyn, M. Samoc, J. W. Wu, A. Attias, J. C. Ribierre, F. Mathevet, *Org. Electron.* **2014**, *15*, 943.

[49] D. Zeng, I. T. Djebbar, Y. Xiao, F. Kameche, N. Kayunkid, M. Brinkmann, D. Guillon, B. Heinrich, B. Donnio, D. A. Ivanov, E. Lacaze, D. Kreher, F. Mathevet, A. J. Attias, *Macromolecules* **2014**, *47*, 1715.

[50] Y. Xiao, X. Su, L. S. Vargas, E. Lacaze, B. Heinrich, B. Donnio, D. Kreher, F. Mathevet, A. J. Attias, *CrystEngComm* **2016**, *18*, 4787.

[51] J. Tang, J. Zhang, Y. Lv, H. Wang, F. F. Xu, C. Zhang, L. Sun, J. Yao, Y. S. Zhao, *Nat. Commun*. **2021**, *12*, 3265.

[52] R. P. Sabatini, F. Maasoumi, S. K. K. Prasad, B. Zhang, C. Clark, T. W. Schmidt, W. W. H. Wong, G. Lakhwani, *Appl. Phys. Lett.* **2020**, *117*, 041103.

Table of contents entry

we demonstrated, for the first time experimentally, that the orientation of the transition dipole moments is one of the key factors for the accelerating polariton relaxation. These outcomes show that the in-plane orientation of dipole moments is a promising strategy for lowering the BEC threshold mainly related to the polariton relaxation rate.

Keywords: (exciton-polariton; microcavities; liquid crystal; molecular orientation; polariton relaxation)

Tomohiro Ishii[1], *Fatima Bencheikh*[1], *Sébastien Forget*[2], *Sébastien Chénais*[2], *Benoit Heinrich*[3], *David Kreher*[4,5], *Lydia Sosa Vargas*[4], *Kiyoshi Miyata*[6], *Ken Onda*[6], *Takashi Fujihara*[1], *Stéphane Kéna-Cohen*[7], *Fabrice Mathevet*[1,4*], *and Chihaya Adachi*[1,8*]

Enhanced light-matter interaction and polariton relaxation by the control of molecular orientation

ToF figure

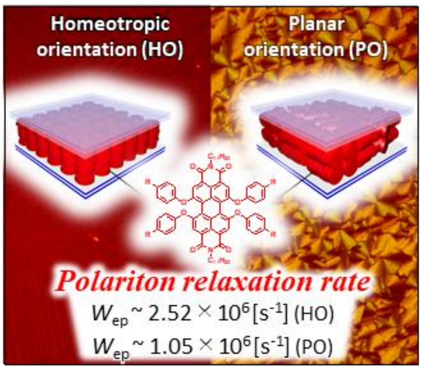

Supporting Information

Enhanced light-matter interaction and polariton relaxation by the control of molecular orientation

Tomohiro Ishii[1], Fatima Bencheikh[1], Sébastien Forget[2], Sébastien Chénais[2], Benoit Heinrich[3], David Kreher[4,5], Lydia Sosa Vargas[4], Kiyoshi Miyata[6], Ken Onda[6], Takashi Fujihara[1], Stéphane Kéna-Cohen[7], Fabrice Mathevet[1,4], and Chihaya Adachi[1,8*]*

Mr. Tomohiro Ishii, Dr. Fatima Bencheikh, Dr. Takashi Fujihara

1. Center for Organic Photonics and Electronics Research (OPERA) and Department of Applied Chemistry, Kyushu University, 744 Motooka, Nishi, Fukuoka 819-0395, Japan.

Prof. Sébastien Forget, Prof. Sébastien Chénais

2. Laboratoire de Physique des Lasers (LPL), Université Sorbonne Paris Nord, CNRS, UMR 7538, F-93430 Villetaneuse, France.

Prof. Benoit Heinrich

3. Institut de Physique et Chimie des Matériaux de Strasbourg (IPCMS), UMR 7504, CNRS-Université de Strasbourg, 23 Rue du Loess, 67034 Strasbourg Cedex 2, France.

Prof. David Kreher,

4. Sorbonne Université, Faculté des Sciences, CNRS, Institut Parisien de Chimie Moléculaire (IPCM), UMR 8232, 4 Place Jussieu, 75005 Paris, France.
5. Institut Lavoisier de Versailles (ILV), UMR-CNRS 8180, Université de Versailles-Saint-Quentin-en-Yvelines, 45 avenue des Etats-Unis, 78035 Versailles cedex, France.

Dr. Lydia Sosa Vargas

4. Sorbonne Université, Faculté des Sciences, CNRS, Institut Parisien de Chimie Moléculaire (IPCM), UMR 8232, 4 Place Jussieu, 75005 Paris, France.

Prof. Kiyoshi Miyata and Prof. Ken Onda

6. Department of Chemistry, Kyushu University, 744 Motooka, Nishi, Fukuoka 819-0395, Japan.

Prof. Stéphane Kéna-Cohen

7. Department of Engineering Physics, École Polytechnique de Montréal, Montréal H3C 3A7, QC, Canada.

Dr. Fabrice Mathevet (E-mail: fabrice.mathevet@sorbonne-universite.fr)

1. Center for Organic Photonics and Electronics Research (OPERA) and Department of Applied Chemistry, Kyushu University, 744 Motooka, Nishi, Fukuoka 819-0395, Japan.

4. Sorbonne Université, Faculté des Sciences, CNRS, Institut Parisien de Chimie Moléculaire (IPCM), UMR 8232, 4 Place Jussieu, 75005 Paris, France.

Prof. Chihaya Adachi (E-mail: adachi@cstf.kyushu-u.ac.jp)

1. Center for Organic Photonics and Electronics Research (OPERA) and Department of Applied Chemistry, Kyushu University, 744 Motooka, Nishi, Fukuoka 819-0395, Japan.

8. International Institute for Carbon Neutral Energy Research (WPI-I2CNER), Kyushu University, 744 Motooka, Nishi, Fukuoka 819-0395, Japan.

Keywords: (exciton-polariton; microcavities; liquid crystal; molecular orientation; polariton relaxation)

1. Perylene bisimide (PBLC) derivative

A. Synthesis

a) General Information

All commercially available chemicals were used without further purification. The 4-nonylphenol used in the second step consisted of a mixture of branched-chain isomers from TCI (CAS RN: 84852-15-3). Solvents used are reagent grade except where specified (NMP, anhydrous, store under molecular sieves. The purifications performed by chromatography/silica plugs were performed using silica gel (Si 60, 40-63 μm, Merck). Nuclear magnetic resonance experiments were recorded on a Bruker® 300, 400, 500 or 600 MHz (ref NMR) equipment from the NMR platform at Sorbonne Université or OPERA laboratory. The proton and carbon chemical shifts (δ) are reported in ppm and are referenced to the residual solvent signal: $CDCl_3$ (7.26).

b) Synthetic route and procedures

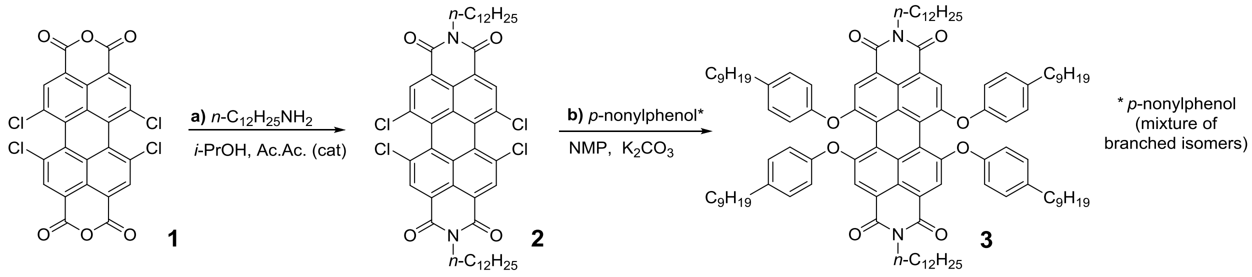

Scheme 1. Reaction conditions for the synthesis of the PBILC derivative. a) *n*-dodecylamine, acetic acid (cat.), reflux (8h) in isopropanol. b) *p*-nonylphenol (mixture of branched isomers) and K_2CO_3, 120°C in NMP (anh.) for 8h.

N, N'bis(n-dodecyl)-1,6,7,12-tetrachloroperylene-3,4,9,10-tetracarboxilic acid bisimide (2)

1,6,7,12-Tetrachloroperylenebisimide (1.06 g, 2 mmol) and *n*-dodecylamine (0.82g, 4.4 mmol) were dissolved in isopropanol (200 ml) and set to stir under an inert atmosphere. A drop of glacial acetic acid is added as catalyst and the mixture is heated to reflux for 4h. The turbid, brick coloured mixture is cooled in an ice bath. Once cool, cold, distilled water (200ml) is added to the mixture to produce a reddish-orange precipitate. The solid is filtered under vacuum and dried. The resulting crude product is passed through a silica-gel plug, using dichloromethane as eluent. The main orange fraction is collected and the solvent removed under reduced pressure to give a bright orange solid (1.27g, 73% yield). ^{1}H NMR (300 MHz, Chloroform-*d*) δ 8.68 (s, 4H, PDI-H), 4.21 (t, *J* = 8.3 Hz, 4H, NCH_2), 1.74 (m, 4H, CH_2), 1.45-1.26 (m, 36H), 0.88 (t, J = 8.0 Hz, 6H).

N, N'bis(n-dodecyl)-1,6,7,12-tetra(4-*i*-nonylphenol) perylene-3,4,9,10-tetracarboxylic acid bisimide (3)

The tetrachlorobis(dodecyl)perylenebisimide **2** (1.25g, 1.45 mmol) was added together with *p*-nonylphenol (4 ml, 17.4 mmol) and K_2CO_3 (1.38 g, 10 mmol) into *N*-methyl-2-pyrrolidone (120 ml, anh.). The reaction mixture is heated to 120°C under an inert atmosphere and left to react for 18h. The resulting dark-purple mixture is cooled to room temperature and an HCl solution (1M, 200 ml) is added to it. The mixture is extracted with dichloromethane, removing a yellow aqueous phase. The red, organic fraction is subsequently washed twice with distilled water (200 ml), before a final wash with an NaOH solution (1M, 200 ml). The resulting organic phase is once again a dark purple colour. This mixture is dried with $MgSO_4$, filtered and the solvent removed under vacuum. The product is purified by passing it through a silica-gel plug using dichloromethane as eluent. A bright red-pink band is recovered as the sole fraction, leaving behind a purple-black baseline. The solvent is removed under vacuum to obtain the title product as a cherry-red, pasty solid (1.4g, 61% yield). NMR characterization is not straightforward, due to the presence of a mixture of branched chain isomers of unknown ramified structure. ^{1}H NMR (300 MHz, Chloroform-*d*) δ 8.19 (m, 4H, PDI-H), δ 7.19 (m, 8H, Ph-H),), δ 6.83 (m, 8H, Ph-H), 4.09 (s, 4H, NCH_2), 1.80 – 0.5 (m, 122H, CH_2 and CH_3). ^{13}C NMR (125 MHz, Chloroform-*d*) δ 163.3, 155.9, 152.7, 132.7, 128.3, 128.2, 127.9, 127.5, 127.2, 122.5, 119.3, (Branched alkyl chains give numerous NMR shifts between 51.9 and 8.8 ppm. Here, we give only the more intense ones) 51.1, 40.6, 31.1, 29.6, 29.5, 29.3, 28.1, 27.1, 22.7, 14.1, 8.8.

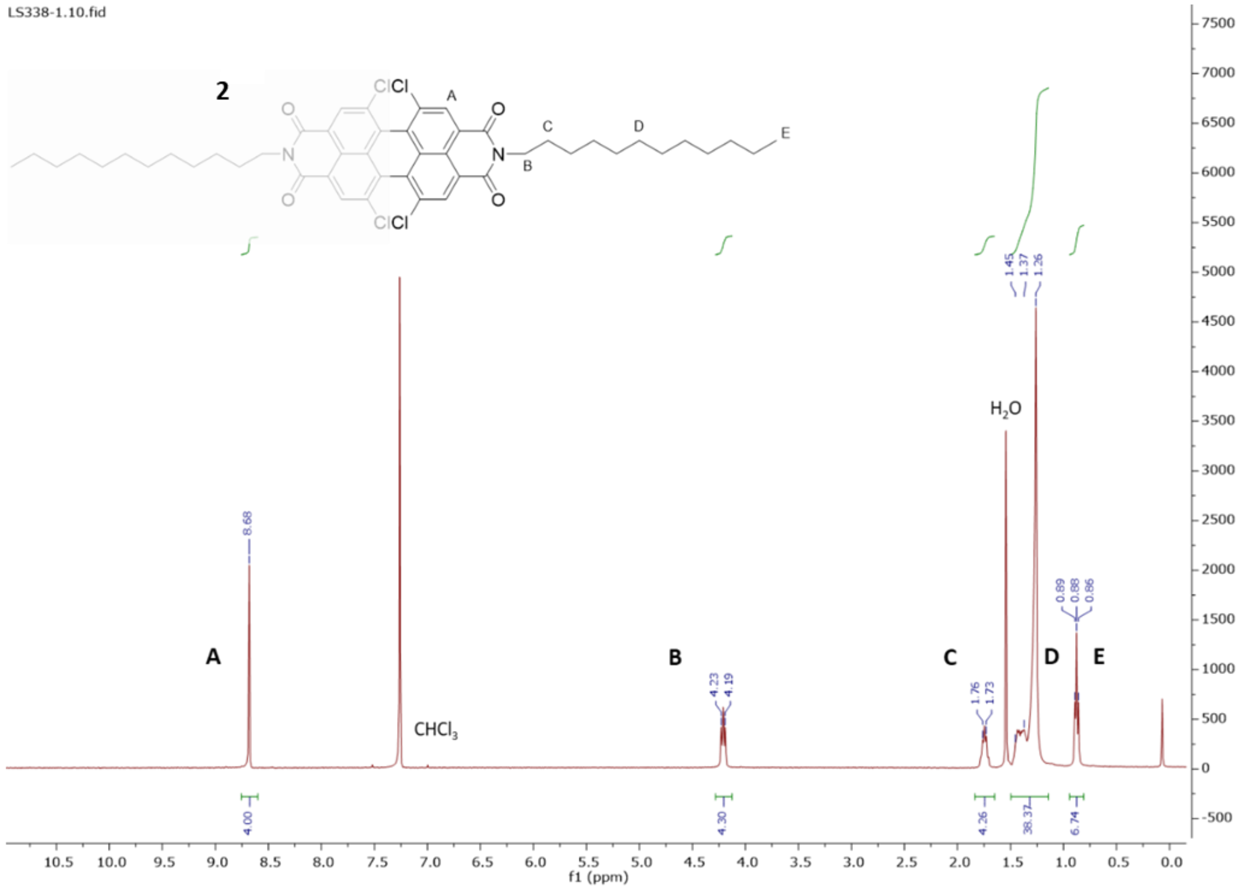
LS338-1.10.fid
2
Cl
Cl
A
O
N
B
C
D
E
H$_2$O
CHCl$_3$
A
B
C
D
E
8.68
4.23
4.19
1.76
1.73
1.45
1.37
1.26
0.89
0.88
0.86
4.00
4.30
4.26
38.37
6.74
f1 (ppm)
10.5 10.0 9.5 9.0 8.5 8.0 7.5 7.0 6.5 6.0 5.5 5.0 4.5 4.0 3.5 3.0 2.5 2.0 1.5 1.0 0.5 0.0
7500 7000 6500 6000 5500 5000 4500 4000 3500 3000 2500 2000 1500 1000 500 0 -500

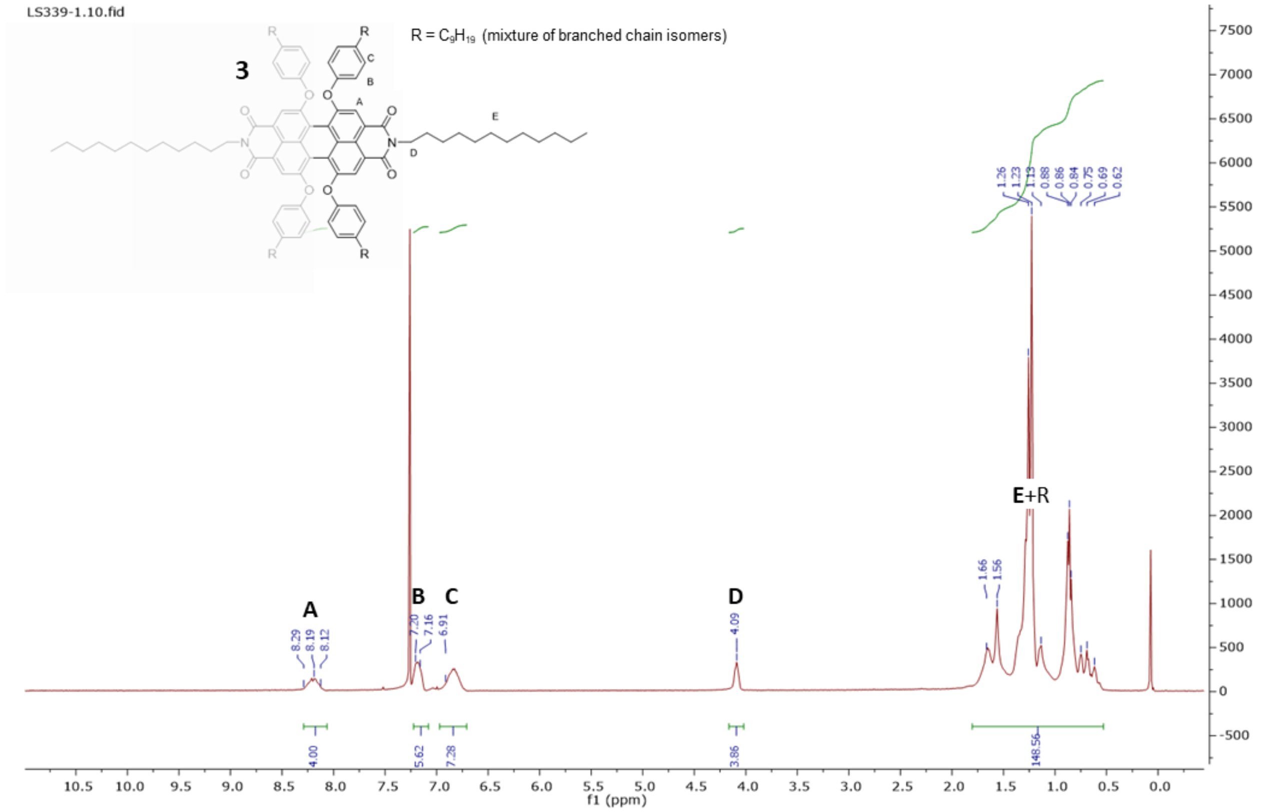
LS339-1.10.fid
3
R = C$_9$H$_{19}$ (mixture of branched chain isomers)
R
A
B
C
D
E
E+R
A
B
C
D
8.29
8.19
8.12
7.20
7.16
6.91
4.09
1.66
1.56
1.26
1.23
1.13
0.88
0.86
0.84
0.75
0.69
0.62
4.00
5.62
7.28
3.86
148.56
f1 (ppm)
10.5 10.0 9.5 9.0 8.5 8.0 7.5 7.0 6.5 6.0 5.5 5.0 4.5 4.0 3.5 3.0 2.5 2.0 1.5 1.0 0.5 0.0
7500 7000 6500 6000 5500 5000 4500 4000 3500 3000 2500 2000 1500 1000 500 0 -500

B. Optical properties for PBLC

The photophysical properties of the Perylene bisimide derivatives (PBLC) were investigated by UV/Vis and fluorescence spectroscopy (solid line in **Fig. S1**). The absorbance spectrum in dichloromethane (DCM) have 0→0 and 0→1, 0→2 transition band with maximum wavelength at 577 nm, 539 nm and 449 nm. The emission spectrum is approximatively the mirror image of absorption spectrum with maximum wavelength at 616 nm and a Stokes shift is about 39 nm. On the other hand, the absorbance and fluorescence spectra of PBLC in solid state show only a small bathochromic shift (about 7nm) and only minor change in the band shapes upon aggregation (dotted lines in **Fig. S1**) This shows that excitonic coupling between molecules is weak in the room-temperature columnar mesophase.

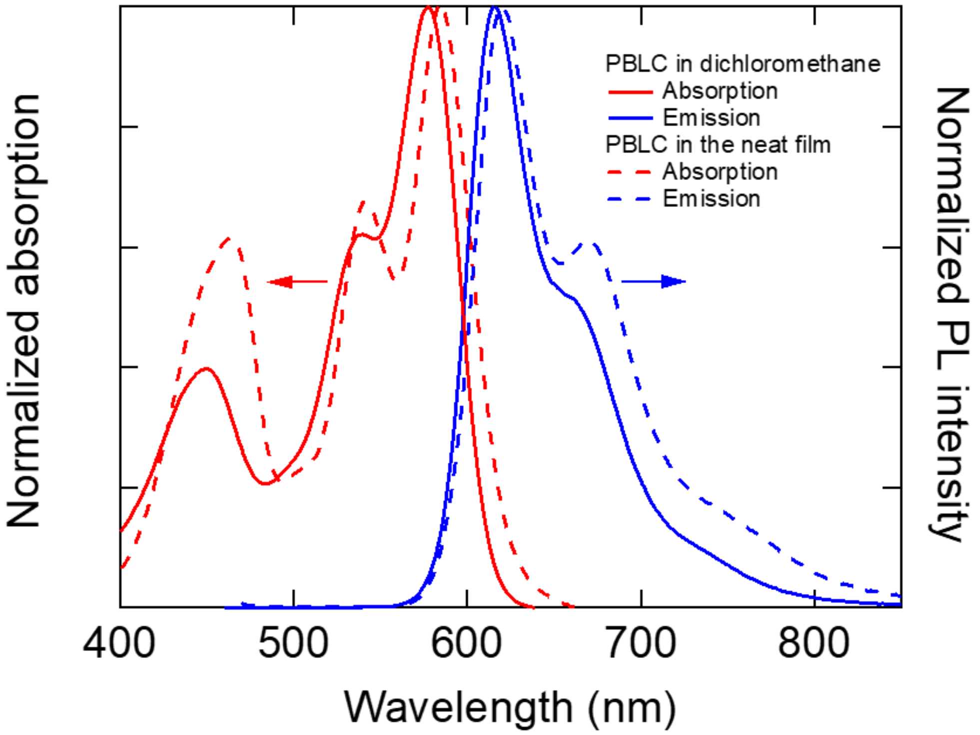

Figure S1. Absorption and Photoluminescence spectra for perylene bisimide (PBLC) derivative in dichloromethaneand spin-coated neat film.

C. Polarizing optical micrograph

Fig. S2a exhibits a polarized optical microscopy (POM) image under the crossed Nicol conditions in the mesophase of PBLC between glass substrate and cover glass at 150℃. The color of imcage partially changes owing to a strong birefringence induced by the columnar orientation of PBLC. In this POM image, the dark area shows the homeotropic alignment of PBLC column and the bright area shows the planar alignment of PBLC column. Also, these structures of columnar phase were maintained at room temperature as shown in **Fig. S2b**.

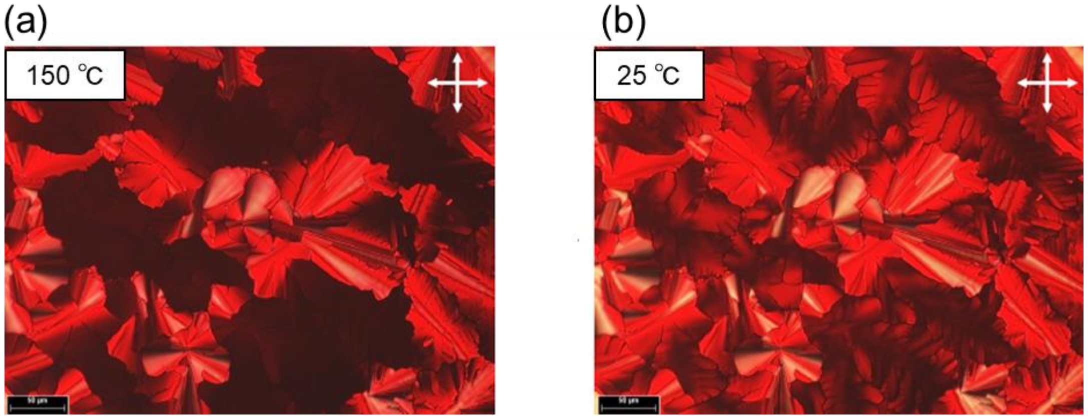

Figure S2. Polarized optical microscopy (POM) image under the crossed Nicol condition in the mesophase of the PBCL between glass substrate and cover glass at (a) 150℃ and (b) room temperature.

2. Quartz/PBLC/quartz structures

A. Fabrication process

To control the domain structure of homeotropic and planar alignment in the mesophase of PBLC, melt grown PBLC thin film sandwiched between two quartz mirrors were fabricated (**Fig. 2** (a) of main text).[1] Homeotropic alignment was fabricated in below process. First, two 100 nm thick gold stripes were deposited on the edges of each quartz plate, then these quartz plates were positioned face to face with their gold stripes aligned and 200 MPa of pressure was applied with mechanical press for 5 min. This resulted in approximately 200 nm-thick, empty cavity channels. The thickness of this empty cavity was estimated by measuring transmittance spectrum. Secondly, upon melting PBLC powder in a nitrogen atmosphere at 200 ℃, liquid PBLC penetrated the channels by capillary action and was crystallized by decreasing the temperature at a rate of 0.1 ℃/min. On the other hand, planar alignment was obtained by performing the same process using octadecyltrichlorosilane (OTS) treated quartz substrate (**Fig. 2** (a) of main text).

B. Polarizing optical micrograph

Figure S3 (a) – (b) show the polarizing optical microscopy (POM) of melt grown PBLC at room temperature. In this POM image, the dark area shows the homeotropic alignment of column of PBLC and the bright area shows the planar alignment of column of PBLC. As can be seen from POM images, homeotropic and planar alignment of PBLC columnar are dominant in each thin film.

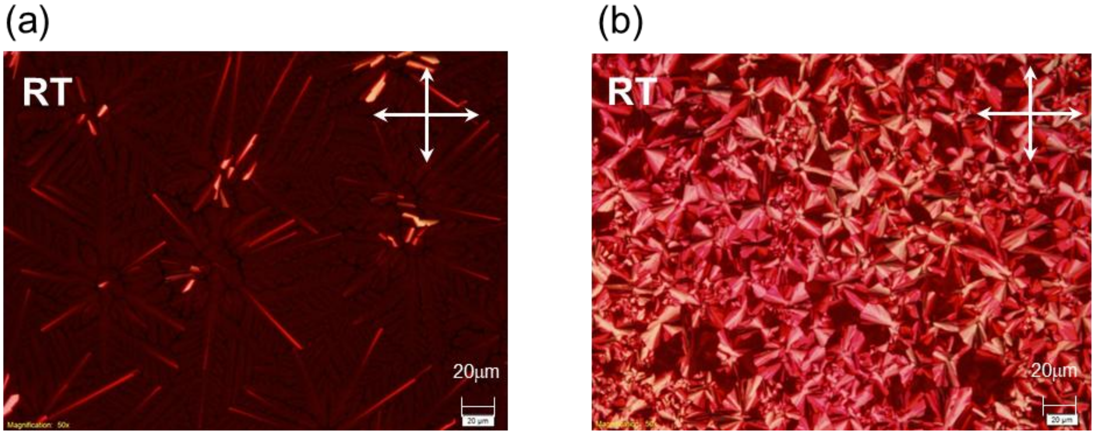

Figure S3. (a) POM image of a multidomain homeotropic texture of PBLC between two clean bare quartz substrates (film thickness ~200 nm). (b) POM image of the multidomain planar texture of PBLC between two octadecyltrichlorosilane-treated (OTS) quartz substrates (film thickness ~200 nm). These images were measured at room temperature.

C. Transition dipole moments for homeotropic and planar alignment

The absorption is proportional to $\left|\vec{\mu}.\vec{E}\right|^2$, which directly derives from the Fermi golden rule. In the face-on homeotropic case, a set of dipoles are randomly oriented but all within a plane that is parallel to the electric field of the incoming radiation (the k vector of impinging light is perpendicular to all dipoles) (Fig. S4 (a)). The absorption coefficient in this case scales as $A_{HO} \sim |\mu|^2|E|^2\langle cos^2\theta\rangle = \frac{1}{2}|\mu|^2|E|^2$ where θ is the angle between the electric field and the transition (absorption) dipole moment. This expression remains true no matter how the electric field (polarization) is oriented within the plane since there is no preferred orientation of the dipoles within the plane here: hence this expression is true for polarized as well as for unpolarized light.

In the edge-on "planar" case, the rotational symmetry is broken (Fig. S4 (b)). There are two angles to consider in 3D: the θ_z angle between the transition moment and the plane (in which the electric field lies, that is the same plane as referenced below, or the plane of DBR mirrors) and the θ_x angle between the projection of the dipole moment in this plane and the electric field direction. If the molecules were having their faces all towards the same direction in space and if linearly polarized light was used for absorption, the θ_x angle would have a fixed value; but here as both unpolarized light is used and several domains exist with different orientations, we can make an average over all possible θ_x orientations as well. As a result, the absorption for the "planar alignment" case is: $A_{PL} \sim |\mu|^2|E|^2\langle cos^2\theta_x\rangle\langle cos^2\theta_z\rangle = \frac{1}{4}|\mu|^2|E|^2$.

Hence, the ratio of absorption theoretically estimated is $\frac{A_{PL}}{A_{HO}} = \frac{1}{2}$, which matches perfectly well the experimental ratio.

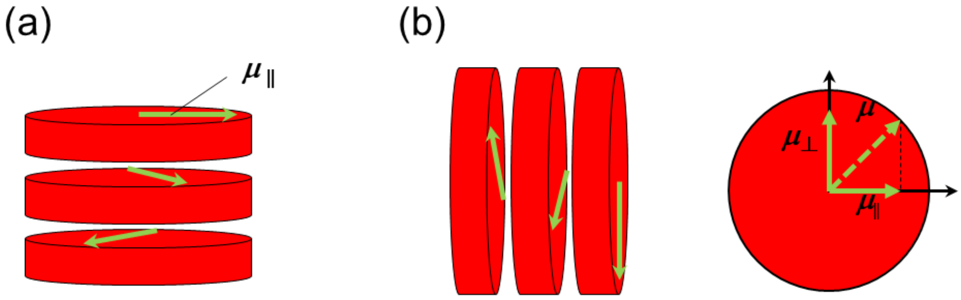

Figure S4. Schematic illustrations of the discotic liquid crystal molecules and direction of transition dipole moments for homeotropic alignment and planar alignment.

3. DBR/PBLC/DBR microcavities

A. Fabrication process and the quality factor

Two types of microcavities containing PBLCs with homeotropic and planar alignment were fabricated by melt grown process, respectively (**Fig. S5**a). [1] Microcavity including homeotropic aligned PBLC was fabricated in below process. First, two 100 nm thick gold stripes were deposited on the edges of each DBR mirror, then these DBR mirrors were positioned face to face with their gold stripes aligned and 200 MPa of pressure was applied with mechanical press for 5 min. This resulted in approximately 270 nm-thick, empty cavity channels. The thickness of this empty cavity was estimated by measuring reflectance spectrum (see **Fig. S6**). Note that the final thickness of the empty cavity is slightly larger than the total thickness of the gold stripes due to the deformation of the quartz substrate of about 35 nm during the high-pressure step for welding the gold stripes (see

Fig. S7). Secondly, upon melting PBLC powder in a nitrogen atmosphere at 200 ℃, liquid PBLC penetrated the channels by capillary action and was crystallized by decreasing the temperature at a rate of 0.1 ℃/min. Also, planar alignment was obtained by performing the same process using octaoctadecyltrichlorosilane (OTS) treated DBR mirror.

From images of POM, a multidomain aligned PBLC texture were confirmed at room temperature as shown in **Figs. S5**b-c, respectively.

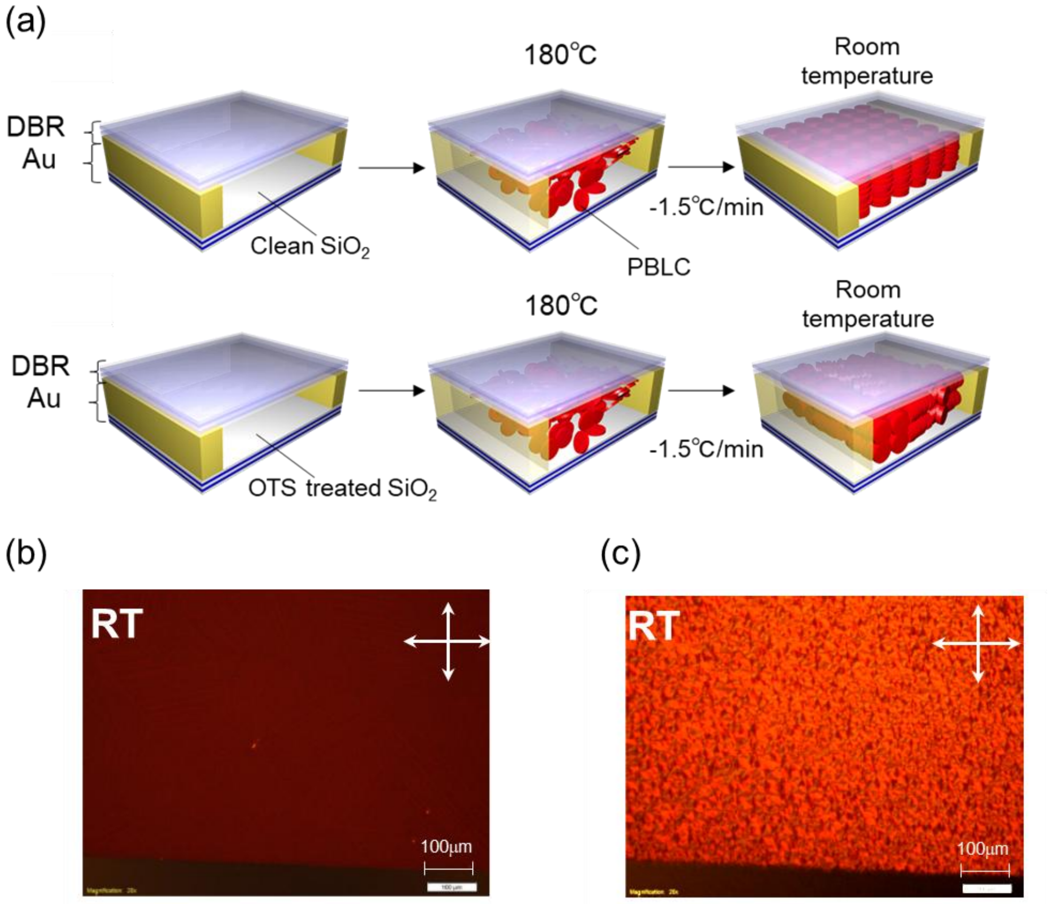

Figure S5. (a) Fabrication by melt processing of microcavities containing (top) a homeotropic alignment of PBLC between two clean DBR substrates and (bottom) a planar alignment by using two octadecyltrichlorosilane (OTS) treated DBR substrates. (b) POM image of homeotropic texture of PBLC in the microcavity. (c) POM image of planar texture of PBLC in the microcavity.

The Q value of the fabricated resonator was determined from FWHM of the dip structure of the reflection spectrum in the empty cavity, DBR/Air/DBR (**Fig. S6** a-b).

$$Q = \frac{\lambda_c}{\Delta\lambda} \sim 200\#(S\mathbf{2})$$

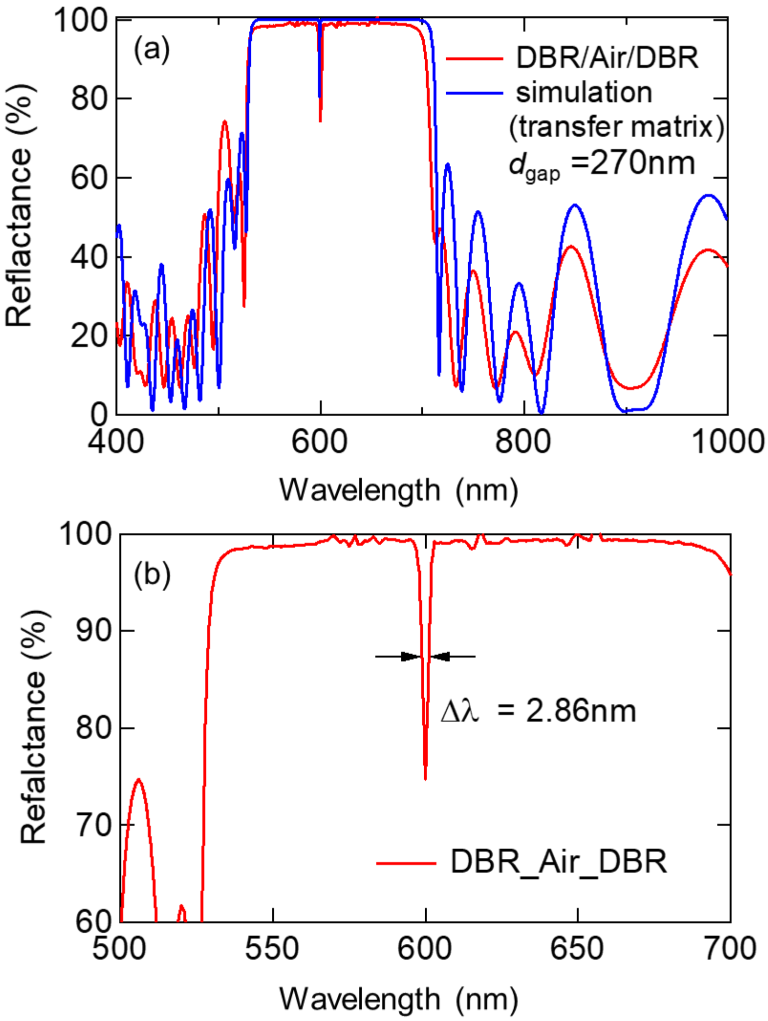

Figure S6. (a) Reflectance spectrum of empty $\lambda/2$ microcavity (DBR/Air/DBR). Thickness of this empty cavity was 270nm from transfer matrix simulation. (b) Expanded reflectance spectrum of empty cavity in the wavelength range of 500 nm to 700 nm.

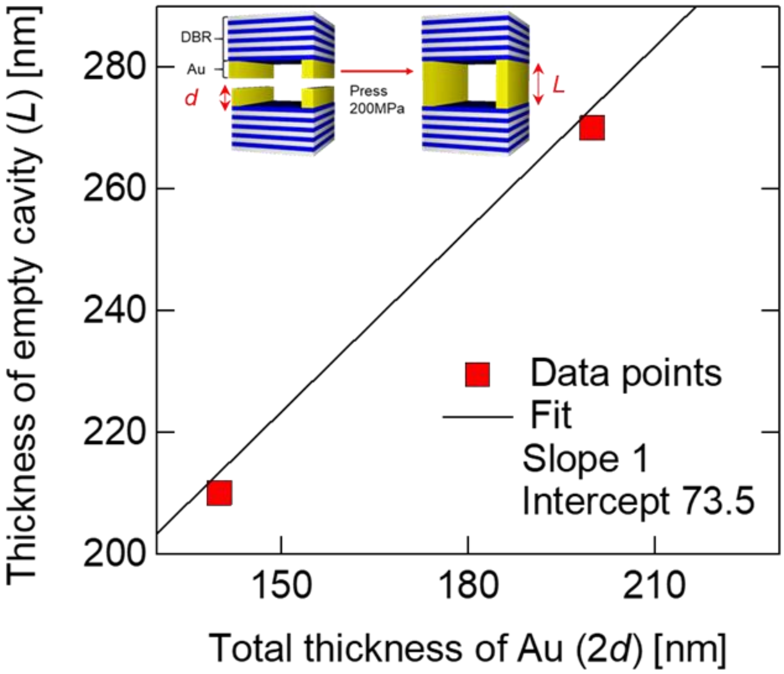

Figure S7. Relationship of the final thickness of the empty cavities with the total thickness of the gold stripes. The data points are fitted with a straight line with a slope of 1 that intercepts the Y-axis at 73.5 nm (for a virtual gold thickness of 0 nm), corresponding to a quartz substrate deformation of about 35 nm.

4. Polariton properties in the microcavities of DBR/PBLC/DBR

A. Angle resolved reflectivity spectra for TM mode

Angle resolved reflectivity spectra for transverse magnetic polarization for MC-HO and MC-PL as shown in **Figs. S8**a-b, respectively. In both microcavities, three peaks are found to anticross around vibronic resonances of $E_{ex}^{0-0} = 2.11\ \mathrm{eV}$, $E_{ex}^{0-1} = 2.29\ \mathrm{eV}$ with increasing angles. These are a characteristic behavior indicating a strong coupling state and associated with the lower polariton (LP), middle polariton (MP) and upper polariton (UP) branches. The dashed blue line in **Fig. S8** show dispersions simulated by a coupled harmonic Hamiltonian (see **Fig. 4** of main text).

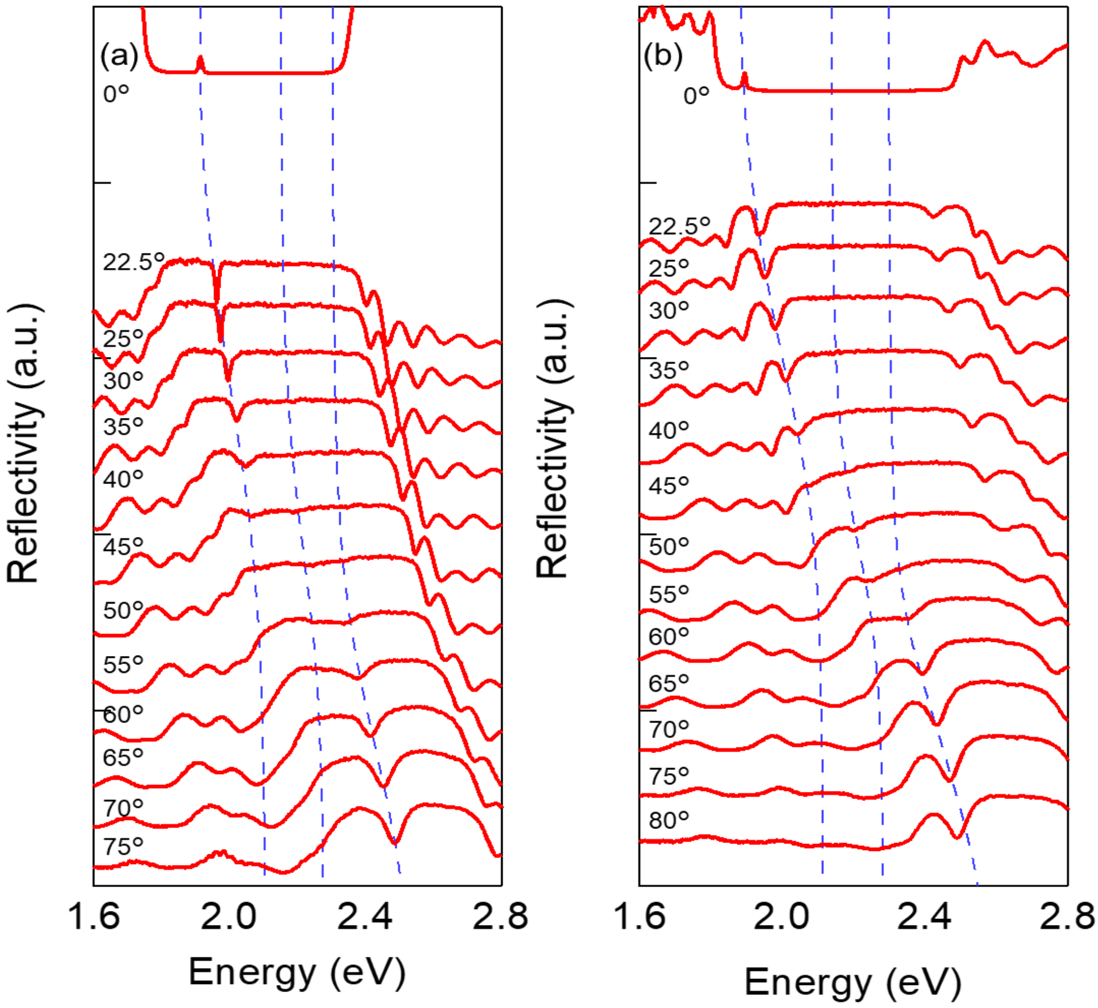

Figure S8. Angle resolved reflectivity spectra measured MC-HO (a) and MC-PL (b), respectively.

B. Contour maps of the angle-resolved reflectivity for TE wave for MC-HO and MC-PL

Figure S9 show a contour map of the transverse electric (TE) measured for MC-HO and MC-PL, respectively. The squares show the dip position identified on the reflectance spectrum for each angle. These dip peaks are found at anti-cross around vibronic resonant energy of $E_{\mathrm{ex}}^{0\text{-}0}$ = 2.11 eV for PBLC. These are a characteristic behavior indicating strong coupling state and associated with the lower polariton (LP) band. Upper polariton and middle polariton were not observed in the high-angle region due to the high reflectance of top mirror. However, since the energies of E_{ph} (0) in TM and TE mode match, we concluded that the resulting dip structures are derived from the lower polaritons. The resulting fit parameters are shown in the inset of **Fig. S9**. And then, the Rabi splitting energies between LP and MP for MC-HO and MC-PL are estimated to be $\hbar\Omega_{HO}^{TE} = 180 \pm 5$ meV and $\hbar\Omega_{PL}^{TE} = 125 \pm 5$ meV, respectively.

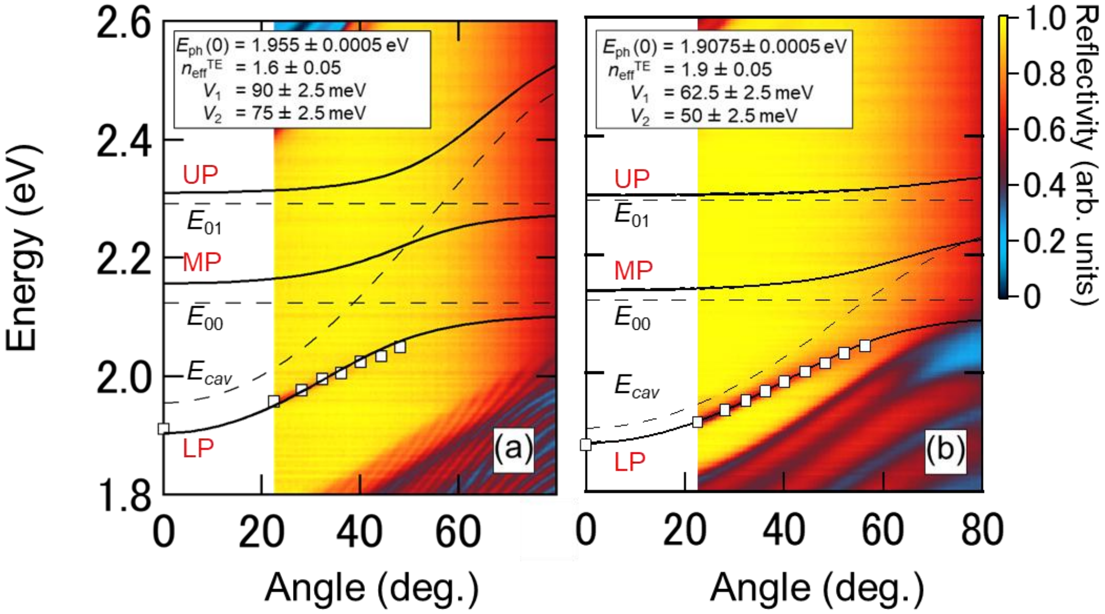

Figure S9. Contour maps of the angle-resolved reflectivity for transverse electric polarization for MC-HO (a) and MC-PL (b). The position of individual minima identified on the spectra are shown as white square dots for each angle. The black solid lines are a fit to a 3-body coupled harmonic oscillator Hamiltonian (CHO). Also, the dashed black line show the dispersion of the uncoupled exciton ($E_{\mathrm{ex}}^{0\text{-}0}$ = 2.11 eV , $E_{\mathrm{ex}}^{0\text{-}1}$ = 2.29 eV) and cavity photon dispersion obtained from CHO. The resulting fit parameters are shown in Fig S9 (inset).

5. Analysis of transient PL data in an microcavity

A. Classical model for calculation of radiative effects

Kevin G. Sullivian *et al.* formulated a classical model for the calculation of radiative effects for a source in the presence of a planar microcavity using a Green's function technique and the plane-wave spectrum in Ref. 2. This method enables to calculate the damping rate of a light source confined inside a 1D planar cavity.

The dipole source is modeled as a harmonically bound charge with a dipole moment p that obeys the equation of motion:

$$\ddot{p} + \omega_0^2 p = \left(\frac{q^2}{m}\right) E_R - b_0 \dot{p} \# (S3)$$

where ω_0 is the resonance angular frequency in the absence of all damping, q is the effective charge, m is effective mass, E_R is the component of the reflected field parallel to the dipole-moment orientation, and b_0 is the damping constant in the absence of reflecting structure. The dipole moment p and reflected field component E_R oscillate at the same complex frequency, $\Omega = \omega - ib/2$:

$$p = p_0 \exp(-i\Omega t) = p_0 \exp\left(-(i\omega + b/2)t\right) \# (S4)$$

$$E_R = E_0 \exp\left(-i\Omega t\right) \# (S5)$$

where ω and b are the resonance frequency and damping rate in the presence of the nearby structure, respectively. Also, the damping rate in the absence of a local structure is given by below formula.

$$b_0 = n_0 \left(\frac{q^2 \omega_0^2}{6\pi \epsilon_0 m c^3}\right) \frac{1}{\gamma} \#\# (S6)$$

where n_0 is refractive index of emitter layer and γ is the quantum yield. The fraction of damping rate between b and b_0 (radiative effect) can be calculated by the interaction between the dipole moment embedded in a microcavity and the reflected field strength and can be represented using effective amplitude-reflection coefficient Γ.

$$\frac{b}{b_0} = 1 + \gamma Re(\Gamma)\#(S7)$$

Γ is related to the reflected field and consists of TE and TM polarized waves. Also, since this effect also depends on the direction of the dipole moment, Γ needs to be considered separately for the case of vertical electric dipole (VED) and horizontal electric dipole (HED).

For generality, effective amplitude-reflection coefficient Γ was examined for the system depicted in **Fig S10** in Ref. 2. This model assumes that the dipole moment embedded in region1 located at position xs. ρ_{12} and ρ_{13} are the amplitude-reflection coefficients associated with region 2 and 3. These coefficients can be calculated with transfer-matrix methods. From Ref. 2, an expression for the effective amplitude reflection coefficient for the VED case is written as

$$\Gamma_{VED} = \frac{3}{2}\int_0^{\infty} du \frac{u^3}{\sqrt{1 - u^2}} \left\{ \frac{\left(1 + \rho_{12}^{TM}\exp(2ik_{1x}x_S)\right)\left(1 + \rho_{13}^{TM}\exp(2ik_{1x}x_D)\right)}{1 - \rho_{12}^{TM}\rho_{13}^{TM}\exp\left(2ik_{1x}(x_D + x_S\right)} - 1 \right\}\#\#(S8)$$

, where $u = [1 - (k_{1x}/k_1)^2]^{1/2}$ is the normalized transverse wave number and $k_\mathrm{i} = n_i\omega/c$ is the wave vector of layer i. For HED, the TE portion of the effective amplitude reflection coefficient is

$$(\Gamma_{HED})_{TE} = \frac{3}{4}\int_0^{\infty} du \frac{u}{\sqrt{1 - u^2}} \left\{ \frac{(1 + \rho_{12}^{TE}exp(2ik_{1x}x_S))(1 + \rho_{13}^{TE}exp(2ik_{1x}x_D))}{1 - \rho_{12}^{TE}\rho_{13}^{TE}exp(2ik_{1x}(x_D + x_S)} - 1 \right\}\#(S9)$$

and for the TM portion, Γ is

$$(\Gamma_{HED})_{TM} = \frac{3}{4}\int_0^{\infty} du \frac{u(1 - u^2)}{\sqrt{1 - u^2}} \left\{ \frac{(1 - \rho_{12}^{TM}exp(2ik_{1x}x_S))(1 - \rho_{13}^{TM}exp(2ik_{1x}x_D))}{1 - \rho_{12}^{TM}\rho_{13}^{TM}exp(2ik_{1x}(x_D + x_S)} - 1 \right\}\#(S10)$$

In the case of homeotropic alignment, effective amplitude-reflection coefficient for VED (Γ_{VED}) becomes zero because the dipole moments orient in the in-plane direction (**Fig. S10** (b)). Therefore, the normalized damping rate is determined by effective amplitude-reflection coefficient of horizontal electric dipole components.

$$F_p^{MC-HO}(x_s) = \left(\frac{b}{b_0}\right)_{HED} = 1 + \gamma Re(\Gamma_{HED})\#(S11)$$

On the other hand, for planar alignment, the direction of the dipole moments can be assumed to be isotropic (**Fig. S10** (c)). Consequently, b/b_0 is given such that.

$$F_p^{MC-PL}(x_s) = \left(\frac{b}{b_0}\right) = \frac{2}{3}\left(\frac{b}{b_0}\right)_{HED} + \frac{1}{3}\left(\frac{b}{b_0}\right)_{VED} = 1 + \gamma\left\{\frac{2}{3}Re(\Gamma_{HED}) + \frac{1}{3}Re(\Gamma_{VED})\right\} \#(S12)$$

Finally, we calculated the averaged F_p using distribution of electric field inside cavity as weighting function.

$$F_p^{ave} = \frac{\int |\boldsymbol{E}(x)| F_{\boldsymbol{p}}\,(x)\boldsymbol{d}x}{\int |\boldsymbol{E}(x)|\boldsymbol{d}x} \#(S13)$$

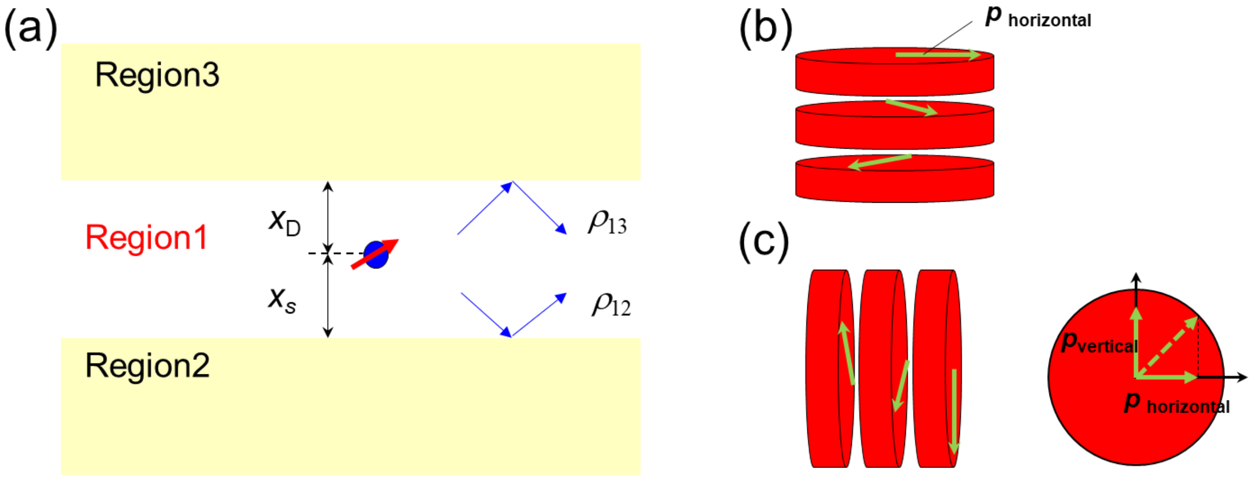

Figure S10. (a) Schematic illustrations of a radiating dipole moment in a planar microcavity. The structures denoted by regions 2 and 3 have associated amplitude coefficients ρ_{12} and ρ_{13}. (b)(c) Schematic illustrations of the discotic liquid crystal molecules and direction of dipole moments for homeotropic alignment and planar alignment.

B. Estimation of F_p for MC-HO and MC-PL

Estimated refractive index and amplitude-reflection coefficients are shown in Table S1. In particular, ρ_{13}^{TE}, ρ_{13}^{TM}, ρ_{12}^{TE} and ρ_{12}^{TM} was calculated for top and bottom DBR mirror using transfer-matrix methods. Note that the phase of the amplitude-reflection coefficient in TE and TM mode is inverted because it is vertically incident light ($\rho_{1i}^{TE}= \rho_{1i}^{TM}$). Also, distribution of electric field was simulated by COMSOL Multiphysics.

In Table S2, F_p^{cal} and F_p^{ex} show the theoretical and experimental values of the normalized damping rate, respectively.

Table S1. Parameters used to calculate effective amplitude reflection coefficient.

Cavity name	ρ_{12}	ρ_{13}	n_1	λ_0 [nm]	d [nm]
MC-HO	0.831+i0.554	0.824+i0.545	1.526+i0.002	647	270
MC-PL	0.717+i0.696	0.695+i0.695	1.478+i0.005	660	270

Table S2. Experimental values of the normalized damping rate

Cavity name	F_p^{cal}	F_p^{ex}
MC-HO	1.04	1.32
MC-PL	1.03	1.19

C. Estimation of PLQY of the lower polaritons

To estimate photoluminescence quantum yield (PLQY) of the lower polaritons, we measured the photoluminescence spectra using an integrating sphere for MC-HO and MC-PL as shown in **Fig. S12**. Blue lines show the integrated excitation spectrum for an empty sphere. In the approach of the absolute method, PLQY is given by.

$$\Phi_{LP} = \frac{\int I_{LP}(\lambda)d\lambda}{\int I_{int}(\lambda) - I'_{int}(\lambda)d\lambda} \#(S14)$$

, where I_{LP} (λ) is the emission spectrum of the lower polariton and $I_{int}(\lambda)$ ($I'_{int}(\lambda)$) is the excitation light spectrum in the absence of the sample (in the presence of the sample). According to this notation, $\int (I_{int}(\lambda) - I'_{int}(\lambda))d\lambda$ corresponds to the number of absorbed photons (Table S3). I_{LP} (λ) was extracted by separating the PL spectrum of MC-HO and MC-PL from the PL spectrum of PBLC.

$$I_{LP}(\lambda) = I_{total}(\lambda) - \left(I_{0-0}(\lambda) + I_{0-1}(\lambda) + I_{0-2}(\lambda) + I_{0-3}(\lambda)\right)\#(S15)$$

Here, the 0-i (i=0, 1, 2, 3) oscillator was assumed a Gaussian as shown in $I_{0-i} = A_i exp(-((\lambda - \lambda_i)/\sigma_i)^2)$. E_{i} and σ_{i} were fixed with the parameters obtained by the fitting of the PL spectrum of the neat films of PBLC (Table. S4, **Fig. S11**). And A_{i} is chosen as a fitting parameter. Note that error bar of PLQYs is obtained from fitting error of Eq. (S15). The contribution of the lower polariton to the PLQY was evaluated by fitting the PBLC microcavity PL spectrum recorded with the integrated sphere by the total spectrum of the LP and the Gaussian distribution of the oscillators 0 - *i* (*i* = 0, 1, 2, 3). The total spectrum of the LP was determined by the bi-gaussian function with the maximum values at 650 nm and 660 nm for MC-HO and MC-PL, respectively (Fig. S13).

Table S3. Parameters used to estimate PLQY of the lower polaritons.

Cavity name	$\int I_{LP}(\lambda)d\lambda$ [a]	$\int I_{int}(\lambda) - I'_{int}(\lambda)d\lambda$ [b]	Absorbance	PLQY [%]
MC-HO	$7.8 \pm 1.6 \times 10^5$	8.2×10^7	0.387	0.96 ± 0.2
MC-PL	$2.7 \pm 0.9 \times 10^5$	6.2×10^7	0.27	0.43 ± 0.15

a) Number of photons in PL emission in the lower polaritons; b) Number of photons in the absorbed excitation light

Table S4. Parameters used to fit of Eq. (14).

Oscillator (0-*i*)	σ_i [nm]	λ_i [nm]
0-0	26.4	631
0-1	24.4	677
0-2	26.7	706
0-3	30	751

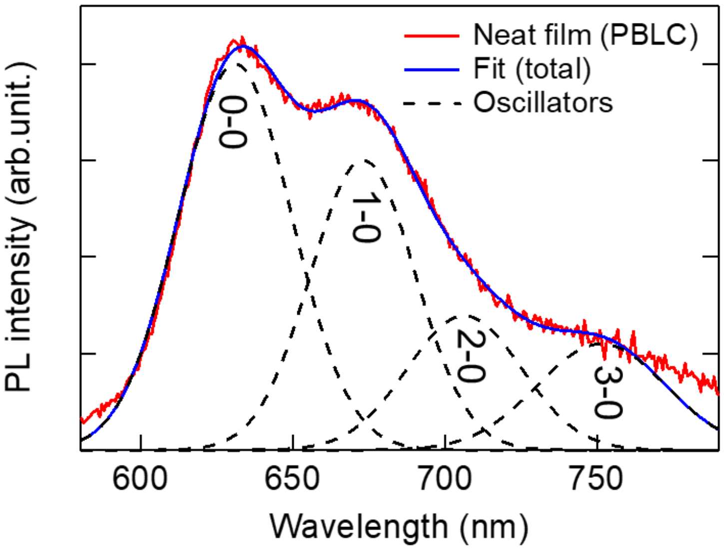

Figure S11. Photoluminescence spectrum of the neat film of PBLC.

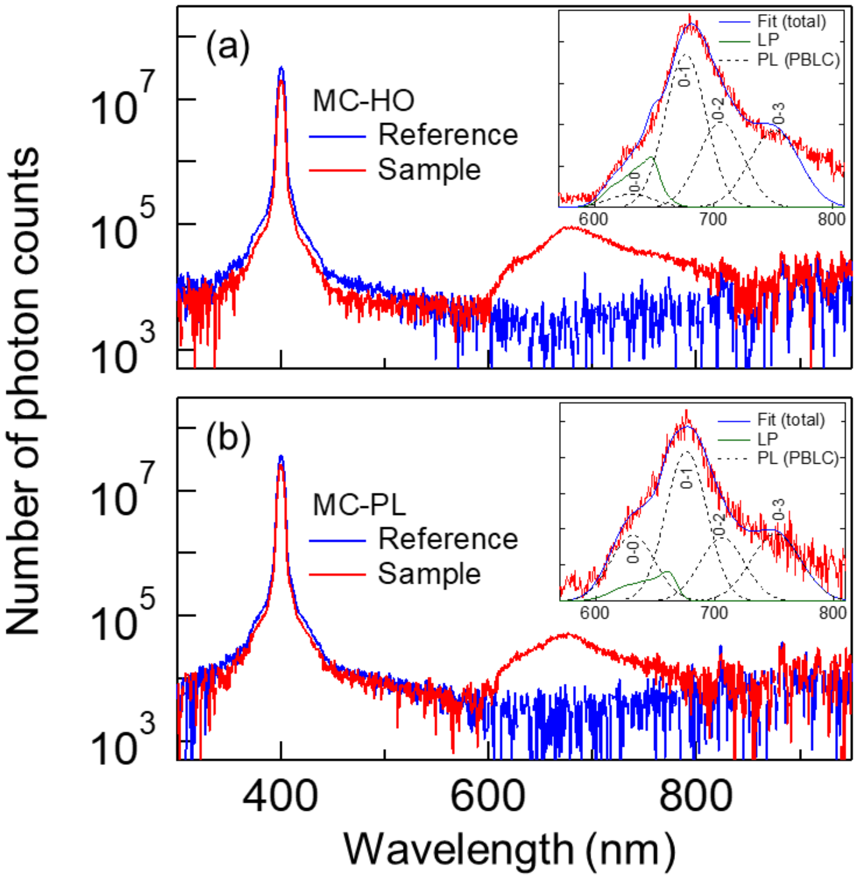

Figure S12. Photoluminescence spectrum of excitation light (blue line) and (a) MC-HO and (b) MC-PL measured by the integrating sphere. Insets show the emission spectrum of samples and fitting results of each oscillator (black dot lines), the lower polaritons (green lines) and superposition of all functions (blue lines).

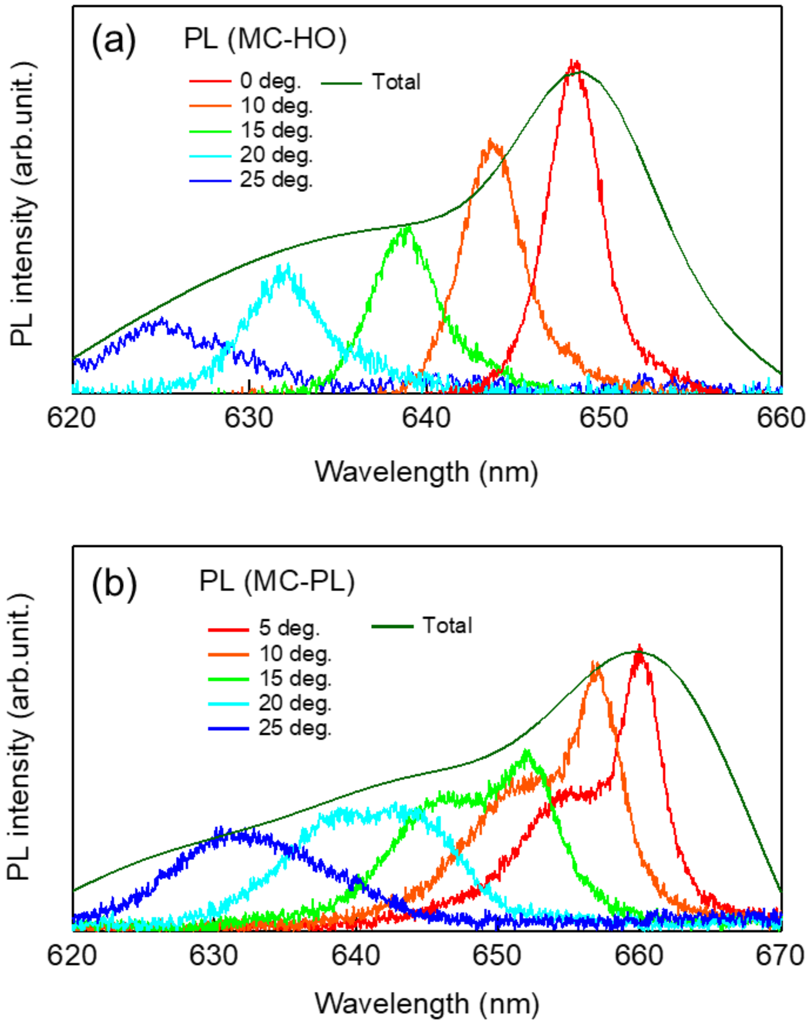

Figure S13. The photoluminescence spectrum of lower polariton for 0° – 25°and the total spectrum (green lines) for MC-HO and MC-PL.

D. Function *f*(*E*) in formula (7) of main text

Function *f*(*E*) is a function of the normalized line shape of (0-1) photoluminescence. First, the (0-1) PL spectrum of PBLC was fitted with the function *g*(*E*).

$$\mathbf{g}(\boldsymbol{E}) = \boldsymbol{A}\mathbf{exp}\left(-\left(\frac{\boldsymbol{E}-\boldsymbol{E_1}}{\boldsymbol{\sigma_1}}\right)^{\mathbf{2}}\right)\#(\mathbf{S15})$$

As shown by the solid blue line in **Fig. S14**, this calculation well agrees with the PL data at fitting parameter of A = 0.65, E_1 = 1.85 eV, σ_1=0.077 eV. Finally, *f*(*E*) was obtained by normalizing *g*(*E*) by its area.

$$\boldsymbol{f}(\boldsymbol{E}) = \boldsymbol{g}(\boldsymbol{E})\frac{\mathbf{1}}{\sqrt{\boldsymbol{\pi}}(\boldsymbol{A\sigma_1})}\#(\mathbf{S16})$$

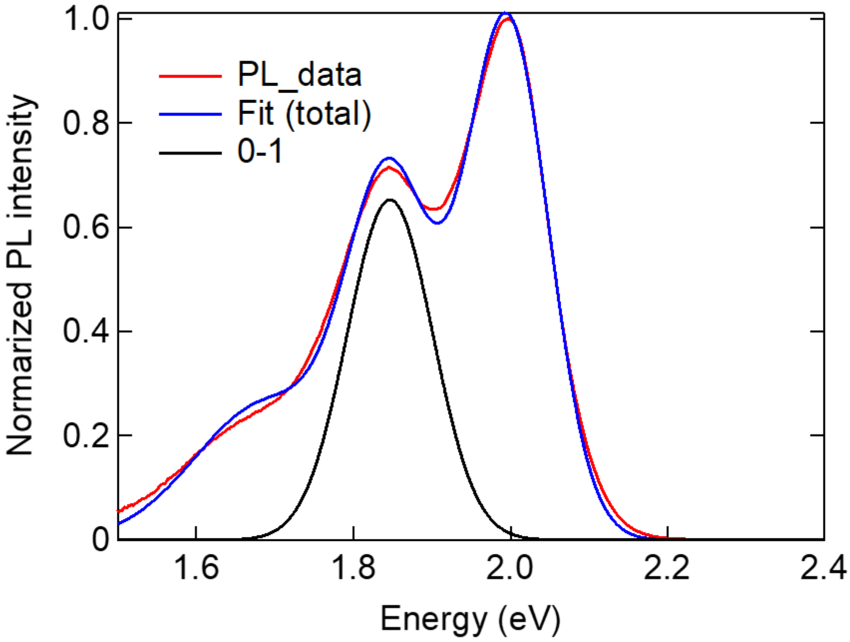

Figure S14. The red solid line is the normalized photoluminescence spectra in the spin coated PBLC neat film of 200 nm. The black solid line is the fits with Gaussian distribution *g*(*E*).

・REFERENCES

[1] S. Kéna-Cohen, M. Davanço, S. R. Forrest, *Phys. Rev. Lett.* **2008**, *101*, 116401.

[2] K. G. Sullivan, D. G. Hall, *J. Opt. Soc. Am. B* **1997**, *14*, 1149.